

1 **Basinal hydrographic and redox controls on selenium enrichment and isotopic composition in**  
2 **Paleozoic black shales**

3  
4 Michael A. Kipp<sup>a,b,\*†</sup>, Thomas J. Algeo<sup>c,d,e</sup>, Eva E. Stüeken<sup>b,f</sup>, Roger Buick<sup>a,b</sup>

5  
6 <sup>a</sup> Department of Earth & Space Sciences and Astrobiology Program, University of Washington,  
7 Seattle, WA, 98195-1310, USA

8 <sup>b</sup> Virtual Planetary Laboratory, NASA Nexus for Exoplanet System Science, Seattle, WA, 98195-  
9 1310, USA

10 <sup>c</sup> Department of Geology, University of Cincinnati, Cincinnati, OH 45221-0013, USA

11 <sup>d</sup> State Key Laboratory of Biogeology and Environmental Geology, China University of  
12 Geosciences, Wuhan 430074, China

13 <sup>e</sup> State Key Laboratory of Geological Processes and Mineral Resources, China University of  
14 Geosciences, Wuhan 430074, China

15 <sup>f</sup> School of Earth & Environmental Sciences, University of St. Andrews, St. Andrews, Fife, KY16  
16 9AL Scotland, United Kingdom

17 \*correspondence to [mkipp@caltech.edu](mailto:mkipp@caltech.edu)

18 †Present address: Division of Geological & Planetary Sciences, California Institute of Technology,  
19 Pasadena, CA, 91125, USA  
20

21 **Abstract**

22 Mass-dependent variations in selenium stable isotope ratios have recently been developed as a  
23 paleo-redox proxy. Since the reduction of selenium oxyanions occurs at a relatively high redox  
24 potential, this system holds promise for probing conditions relevant to the evolution and  
25 diversification of eukaryotic and animal life, which required substantial dissolved oxygen levels.  
26 Although several studies have identified selenium isotopic variability during oxygenation events  
27 in Earth's distant past, we still have only a broad understanding of the mechanisms controlling  
28 this isotopic variability. This currently limits the robust interpretation of selenium isotope  
29 variability to first-order mechanisms driving large-magnitude changes. Here, we explore  
30 selenium isotope variability within and among Paleozoic black shales deposited on the North  
31 American craton that have been well-studied using a variety of other paleo-environmental  
32 proxies. Using this combined dataset, we attempt to unravel the controls on selenium abundance  
33 and isotope ratios in organic-rich ancient marine sedimentary rocks. We find that in the Late  
34 Pennsylvanian units, an estuarine nutrient trap on the Midcontinent Shelf enabled vigorous  
35 selenium recycling, leading to very high concentrations in sediments and enrichment of heavy  
36 isotopes in the aqueous selenium reservoir. In contrast, we find that among the Late Devonian  
37 units, differences in local basinal hydrography led to a gradient in selenium abundance and  
38 isotopic fractionation, with the more restricted basins depleting their selenium reservoirs and  
39 causing enrichment of heavy isotopes in the residual aqueous reservoir. In both of these case  
40 studies, the additional context provided by complementary paleo-environmental proxies was  
41 critical for distinguishing between possible drivers of selenium isotopic variability. When  
42 extending such studies to other paleo-environmental settings, we suggest that the continued use  
43 of complementary datasets will enable the most robust use of the selenium paleo-redox proxy.  
44 Moreover, further development of techniques for high-precision and phase-specific selenium

45 isotope measurements will greatly improve the ability to deduce subtle redox fluctuations with  
46 this proxy.

47

48 *Keywords:* selenium isotopes; epicontinental seas, late Paleozoic; basin hydrography; redox  
49 proxies; redox-sensitive trace elements

## 50 1. Introduction

51 Evaluating the redox state of ancient seawater is a key aspect of studying Earth's  
52 environmental evolution. This task is critical to the study of rising oxygen levels throughout  
53 geologic history (*e.g.*, [Lyons et al., 2014](#)), environmental triggers of early animal evolution (*e.g.*,  
54 [Sperling et al., 2013](#)), kill mechanisms of mass extinction events (*e.g.*, [Wignall and Twitchett,](#)  
55 [1996](#)), and even oceanographic mechanisms of carbon storage on glacial-interglacial timescales  
56 (*e.g.*, [Anderson et al., 2019](#)). As such, the paleoceanographic toolkit is always being refined to  
57 include novel paleo-redox proxies with ever-more precise informative power.

58 Over the last two decades there has been a surge of interest in trace element proxies for  
59 paleo-redox conditions ([Tribovillard et al., 2006](#); [Anbar and Gordon, 2008](#); [Algeo et al., 2012](#);  
60 [Little et al., 2015](#)). Studies of redox-sensitive trace metal enrichment have proven greatly  
61 informative of first-order secular trends in Earth's stepwise oxygenation ([Scott et al., 2008](#); [Partin](#)  
62 [et al., 2013](#)) and transient anoxic events in the more recent past ([Brumsack, 2006](#)). Taking this a  
63 step further, the field of "non-traditional" stable isotope geochemistry has recently grown into a  
64 discipline of its own (*e.g.*, [Teng et al., 2017](#)), creating a potentially richer source of information  
65 about oxidation-reduction reactions in a variety of paleo-environmental settings.

66 Some redox-sensitive trace element isotopic systems have already yielded a wealth of  
67 information about modern and ancient redox processes in seawater. For instance, molybdenum  
68 (Mo) isotopes in sulfidic black shales have become a well-established proxy for the global extent  
69 of sulfidic seawater (*e.g.*, [Siebert et al., 2003](#); [Gordon et al., 2009](#); [Kendall et al., 2017](#)) and have  
70 allowed inferences about the secular oxygenation of the Earth's ocean over billion-year  
71 timescales (*e.g.*, [Arnold et al., 2004](#); [Dahl et al., 2010](#); [Kendall et al., 2011](#); [Chen et al., 2015](#);  
72 [Kendall et al., 2015](#)). Uranium (U) isotopes in carbonates have recently joined Mo as a  
73 quantitatively powerful global-ocean redox proxy, with sensitivity to the areal extent of anoxic  
74 sediments (*cf.* [Tissot and Dauphas, 2015](#)), and they have been used to study a wide range of  
75 events in deep time ([Lau et al., 2016](#); [Lau et al., 2017](#); [Clarkson et al., 2018](#); [Zhang et al., 2018](#);  
76 [Tostevin et al., 2019](#)). An advantage of both the Mo and U proxies is that these elements have  
77 long residence times of  $>10^5$  yr in the modern ocean and therefore have the potential to capture  
78 global redox conditions.

79 In addition to inferences about redox conditions in the global ocean, more localized redox  
80 assessments have been enabled by proxies such as the iodine content of carbonates (Lu et al.,  
81 2010; Lu et al., 2018). As iodate ( $\text{IO}_3^-$ ) is quickly reduced to iodide ( $\text{I}^-$ ) in suboxic water (e.g., Rue  
82 et al., 1997), iodate incorporation in carbonates is only possible under fairly well-oxygenated  
83 waters (Lu et al., 2010). This high redox potential of the iodine system allows interrogation of  
84 redox fluctuations close to thresholds that are relevant to eukaryotic – including animal – life.  
85 However, without multiple stable isotopes the iodine system is less amenable to quantitative flux  
86 reconstructions than its aforementioned counterparts.

87 Although the above proxies all have demonstrable power in evaluating redox conditions  
88 in ancient seawater, there are gaps in their spatial, temporal and redox sensitivities that might  
89 be filled by other trace element systems. The selenium (Se) system is promising in this respect,  
90 since the high redox potential of Se oxyanion reduction is similar to that of iodate and nitrate  
91 (e.g., Rue et al., 1997; Fig. 1). Furthermore, the marine residence time of Se ( $10^3$ - $10^4$  yr) is of a  
92 similar order of magnitude to the ocean mixing time (Broecker and Peng, 1982), and possibly  
93 much shorter under anoxic conditions, meaning that it is likely not globally homogenized and  
94 thus yields more localized redox information than the Mo and U systems. Selenium isotopes  
95 should therefore respond to global and regional perturbations on relatively short timescales.  
96 With six stable isotopes and an ability to shift between the -II, 0, +IV and +VI oxidation states in  
97 seawater (Cutter and Bruland, 1984), the Se system has the potential to encode a wealth of  
98 information about redox reactions in the marine environment. Despite this potential, Se isotopes  
99 remain much less studied than the aforementioned proxies.

100 There are several factors that conspire to make Se a difficult system to investigate.  
101 Selenium volatilization during wet chemical sample preparation can alter Se concentrations and  
102 isotopic compositions (Chau and Riley 1965; Kurzawa et al., 2017), requiring vigilance during  
103 digestion and evaporation. Furthermore, Se is typically introduced to the MC-ICP-MS via a  
104 hydride generator (HG-MC-ICP-MS) in order to improve signal strength, but this apparatus can  
105 be a source of signal instability (Rouxel et al., 2002). Even following successful introduction to the  
106 plasma, Se measurements are complicated by isobaric interferences from germanium, arsenic,  
107 krypton and – most insidiously – argon (Ar), which confounds analysis of the most abundant Se

108 isotope ( $^{80}\text{Se}$ ) through interference with Ar dimers (reviewed in [Stüeken et al., 2013](#)). Beyond  
109 these analytical challenges, Se is generally present at low abundances in geological materials  
110 (ng/g to  $\mu\text{g/g}$ ; [Rouxel et al., 2002](#); [Mitchell et al., 2012](#); [Stueken et al., 2015](#); [Kurzawa et al., 2017](#)),  
111 often requiring the digestion of large amounts of sample to obtain sufficient Se for analysis.  
112 Despite these complications, however, recent methodological developments in both the  
113 chemical preparation and analytical environment of Se isotope analysis have successively pushed  
114 this system toward the realm of routine analysis (*e.g.*, [Stüeken et al., 2013](#); [Pogge von](#)  
115 [Strandmann et al., 2014](#); [Kurzawa et al., 2017](#)), opening up the possibility that Se isotopes can  
116 soon enter the standard toolkit of paleoceanographers.

117         Although these techniques have enabled the study of Se isotopic variability in a wide  
118 range of settings (*e.g.*, soils, [Schilling et al., 2011](#); groundwater, [Basu et al., 2016](#); lakes, [Clark and](#)  
119 [Johnson, 2010](#); laboratory, [Johnson and Bullen, 2003](#); [Ellis et al., 2003](#)), large gaps remain in our  
120 understanding of the behavior of Se and its isotopes across redox gradients in the modern ocean  
121 and during (de-)oxygenation events in Earth's past. Here, we leverage a wealth of data from other  
122 redox-sensitive elements to better evaluate the similarities and differences between the Se  
123 system and other proxies. Specifically, we focus on two sample sets of well-characterized black  
124 shales deposited on the North American continent during the late Paleozoic Era in two intervals:  
125 (a) the Late Pennsylvanian and (b) the Late Devonian. We measured Se concentrations and  
126 isotopic ratios in 65 samples from these units and compared the data to a variety of paleo-  
127 environmental indicators. In particular, we sought to determine the effects of watermass  
128 restriction and local redox conditions on Se abundance and isotopic fractionation in these two  
129 settings. In doing so, we aimed to elucidate the mechanisms responsible for the observed  
130 variability in Se isotope ratios and enrichment factors among the study units, with broader  
131 implications for the further development of Se as a paleoceanographic proxy.

132

## 133 **2. Selenium geochemistry**

### 134 *2.1 The selenium cycle*

135         Selenium is a trace constituent of the upper continental crust, with a mean concentration of  
136  $\sim 60$  ng/g ([Stüeken, 2017](#)). Crustal Se is predominantly found in sulfide minerals, with Se

137 substituting for sulfur. The Se isotopic composition (here and throughout the text reported in  
138 delta notation as  $\delta^{82/78}\text{Se}$  relative to Se NIST SRM 3149; Carignan and Wen, 2007) of the upper  
139 continental crust is estimated to be  $\sim 0.0 \pm 0.5\text{‰}$  (Stüeken, 2017) based on analyses of  
140 representative igneous reservoirs (Rouxel et al., 2002; Kurzawa et al., 2017; Yierpan et al., 2018).  
141 The range of  $\delta^{82/78}\text{Se}$  values observed in bulk marine sediments deposited across all of Earth's  
142 history is approximately  $-3\text{‰}$  to  $+3\text{‰}$  (Stüeken et al., 2015b; Mitchell et al., 2016), indicating  
143 that isotopic fractionation of Se occurs during biogeochemical cycling.

144 The dominant input of Se to the modern ocean is oxidative continental weathering, whereby  
145  $\text{Se}^{\text{II}}$  in crustal sulfides is oxidized to  $\text{Se}^{\text{IV}}$  or  $\text{Se}^{\text{VI}}$ , which form highly soluble oxyanions. The process  
146 of oxidative weathering typically induces rather small isotopic fractionations ( $<0.5\text{‰}$ ; Johnson et  
147 al., 1999; Schilling et al., 2011). Weathering of exceptionally Se-rich shales (up  $\sim 2$  wt. % Se) has  
148 been shown to enable larger fractionations (Zhu et al., 2014), though this wide range is neither  
149 thought to be representative of most weathering environments nor of net global inputs, because  
150 in that particular case secondary Se cycling was facilitated by unusually large amounts of organic  
151 matter in the rocks. Given generally small fractionations during weathering and transport, the  
152 riverine supply of Se to the ocean is thought to have an isotopic composition similar to the upper  
153 continental crust ( $\sim 0\text{‰}$ ). Additional Se input from volcanic gases (which can contain  $\text{H}_2\text{Se}$ ) plays  
154 a minor role in the global Se budget today (Mosher and Duce, 1987; Floor and Román-Ross 2012;  
155 Stüeken, 2017), but could conceivably have been more important early in Earth's history prior to  
156 the onset of significant oxidative continental weathering in the late Archean (Stüeken et al.,  
157 2012). The isotopic composition of volcanic Se has not been directly constrained, but it is thought  
158 that this flux does not substantially alter the marine Se isotope mass balance (Stüeken, 2017).

159 Upon reaching the ocean, Se is scavenged in the photic zone as an essential micronutrient,  
160 yielding nutrient-type profiles in the ocean (Measures et al., 1980; Measures and Burton, 1980).  
161 The biological pump is the dominant vector of Se transport from surface waters to the deep  
162 ocean and marine sediments. Selenium has a short residence time ( $\sim 2\text{-}3$  yr) as Se oxyanions in  
163 surface waters (Cutter and Bruland, 1984) and an intermediate residence time ( $10^3\text{-}10^4$  yr, similar  
164 to oceanic mixing times) as regenerated Se oxyanions in the deep ocean (Broecker and Peng,  
165 1982; Cutter and Bruland, 1984). The bioassimilation of Se by phytoplankton generally imparts a

166 small isotopic fractionation (<0.5‰; [Clark and Johnson, 2010](#)), which may be negligible when  
167 uptake is quantitative. The isotopic composition of Se in planktonic biomass is thus thought to  
168 approximate that of dissolved Se in seawater ([Stüeken et al., 2015b](#); [Stüeken, 2017](#)).

169 Owing to its low concentration (~1-2 nM), there are few direct measurements of Se isotope  
170 ratios in seawater. A recently developed method for determining the concentration and isotopic  
171 composition of Se in seawater yielded  $\delta^{82/78}\text{Se}$  values (scaled from  $\delta^{82/76}\text{Se}$  assuming mass-  
172 dependent fractionation) of +0.27‰ for deep waters of the NW Pacific Ocean ([Chang et al.,](#)  
173 [2017](#)). This closely agrees (within a  $1\sigma$  analytical precision of  $\pm 0.1$ - $0.2\%$ ; cf. [Mitchell et al., 2012](#);  
174 [Stüeken et al., 2015b, 2015c](#); [this study](#)) with a single measurement of phytoplankton biomass  
175 (+0.27‰; [Mitchell et al., 2012](#)), a single measurement of a deep-sea Fe-Mn nodule (+0.32‰;  
176 [Rouxel et al., 2004](#)), and mass balance calculations estimating the Se-isotopic composition of  
177 seawater as ~+0.3‰ ([Stüeken, 2017](#)).

178 Marine sediments are commonly enriched in Se. Sediments deposited in oxic, open-ocean  
179 settings over the last ~500 kyr have an average (geometric mean) Se concentration of 0.68  $\mu\text{g/g}$   
180 (95% confidence interval of 0.55 to 0.83,  $n = 100$ ), whereas sediments deposited in anoxic settings  
181 have systematically higher Se concentrations (geom. mean = 2.18  $\mu\text{g/g}$ ; 95% confidence interval  
182 of 1.46 to 3.27  $\mu\text{g/g}$ ,  $n = 38$ ) (data compiled in [Stüeken et al., 2015b](#)). For this reason, the study  
183 of Se isotopes as a paleo-redox proxy has thus far focused predominantly on reducing marine  
184 sediments, which typically have moderate to high Se concentrations. Our understanding of the  
185 processes controlling Se enrichment and isotopic fractionation in these settings is reviewed  
186 below.

187

## 188 2.2 *The selenium isotope paleo-redox proxy*

189 The removal of Se to marine sediments and fractionation of Se isotopes are driven by multiple  
190 biogeochemical processes. Remineralization of organic matter in sediments results in the release  
191 of some bioassimilated Se, the fate of which is redox dependent. In oxic facies, adsorption of the  
192  $\text{Se}^{\text{IV}}$  ion selenite onto Fe-Mn-oxides can be significant (cf. [Balistrieri and Chao, 1990](#); [Rovira et al.,](#)  
193 [2008](#)). In reducing facies (*i.e.*, the targets of the present study), seawater Se removal follows two  
194 main pathways: (a) the burial of biologically-assimilated Se in organic matter, and (b) the

195 sequestration of Se through dissimilatory reduction of oxyanions to inorganic Se<sup>0</sup> or Se<sup>-II</sup> phases.  
196 The relative importance of these two burial pathways is poorly constrained, though limited  
197 phase-specific Se measurements in modern settings suggest that the resulting Se pools (*i.e.*,  
198 organic-bound Se derived from export production and Se<sup>0</sup> or sulfide-hosted Se<sup>-II</sup> derived from  
199 dissimilatory oxyanion reduction) can comprise roughly similar proportions of total sedimentary  
200 Se (Velinsky and Cutter, 1990).

201 The first route is likely dominated by organic matter exported from the photic zone, where  
202 primary productivity is highest and phytoplankton have a nutritional demand for Se. The second  
203 route chiefly involves reductive immobilization of Se oxyanions liberated from biomass in deep  
204 waters or sediment porewaters. At reduction potentials similar to that of nitrate reduction (Fig.  
205 1), Se oxyanions are reduced first to Se<sup>0</sup> and then potentially further to Se<sup>-II</sup> (Oremland et al.,  
206 1989). Fully reduced Se<sup>-II</sup> can substitute for sulfur in diagenetic sulfide minerals (*e.g.*, pyrite),  
207 which provide a stable host phase for Se on geological timescales due to the stoichiometric  
208 incorporation of Se in the mineral structure (Large et al., 2014, and references therein). Processes  
209 surrounding the burial of Se<sup>0</sup> are less well constrained. Reduction to Se<sup>0</sup> generates nanoparticles  
210 that can sink out of the water column and accumulate in sediments (Oremland et al., 1989;  
211 Velinsky and Cutter, 1990). It is unclear to what extent these particles withstand diagenetic and  
212 metamorphic conditions, but some amount of Se<sup>0</sup> appears to be recoverable from ancient marine  
213 sedimentary rocks (Kulp and Pratt, 2004; Wen et al., 2007). It is likely, though, that subsequent  
214 reduction to Se<sup>-II</sup> on diagenetic timescales enables a considerable degree of Se incorporation into  
215 sulfides, as the Se content of pyrite in ancient marine sedimentary rocks (Kulp and Pratt, 2004;  
216 Fan et al., 2011) far exceeds the amounts detected in modern sediments (Velinsky and Cutter,  
217 1990).

218 The bulk Se isotopic composition of reduced marine sediments is a function of both the  
219 biogenic (*i.e.*, organic-bound) fraction and the reductively immobilized (*i.e.*, elemental and  
220 sulfide-bound) fraction. Due to the generally small isotopic fractionations associated with  
221 biological uptake and remineralization (Johnson and Bullen 2004; Clark and Johnson, 2010), the  
222 Se isotopic composition of biomass in marine sediments is thought to fairly closely match that of  
223 dissolved Se in the surface ocean (~+0.3‰; Mitchell et al., 2012; Stüeken et al., 2015b). In

224 contrast, Se sequestered through oxyanion reduction can become substantially isotopically  
225 lighter than seawater if the process is non-quantitative, as Se reduction exerts a large kinetic  
226 isotopic preference for lighter isotopes (as much as  $-12\text{‰}$ ; [Johnson and Bullen, 2004](#)). Non-  
227 quantitative reduction is thought to be prevalent in sediments with suboxic porewaters or  
228 bottom waters that are connected to a large, oxic reservoir of Se oxyanions, thereby allowing  
229 renewed Se supply and precluding complete consumption of the dissolved Se pool.

230 Modern environments that likely harbor non-quantitative Se reduction include open-marine  
231 settings such as the mid-Atlantic ([Johnson and Bullen, 2004](#)), the Bermuda Rise ([Shore, 2011](#)),  
232 and the Arabian Sea ([Mitchell et al., 2012](#)). Bulk marine sediments from these open-marine  
233 settings over the last  $\sim 500$  kyr are slightly isotopically depleted relative to seawater ( $\delta^{82/78}\text{Se} = -$   
234  $0.10 \pm 0.21\text{‰}$ ,  $n = 100$ ; data compiled in [Stüeken et al., 2015b](#)), likely reflecting minor  
235 fractionation during non-quantitative reduction. The fact that only slight isotopic depletion is  
236 observed in these bulk marine sediments – in contrast to the large isotopic effects (up to several  
237 per mille) seen in laboratory settings ([Johnson and Bullen, 2004](#)) – may partly derive from dilution  
238 of the isotopically depleted signal (which is likely retained in the elemental and/or sulfide phase)  
239 by unfractionated Se in the organic phase ([Stüeken et al., 2015b](#); [Mitchell et al., 2016](#)). Phase-  
240 specific Se recovery has been explored in a number of studies ([Martens and Suarez, 1997](#); [Kulp](#)  
241 [and Pratt, 2004](#); [Clark and Johnson, 2010](#); [Fan et al., 2011](#); [Schilling et al., 2011](#); [Schilling et al.,](#)  
242 [2014](#); [Stüeken et al., 2015c](#)), but isotopic data on specific phases in marine sedimentary rocks are  
243 limited to a single sample from a study of end-Permian shales ([Stüeken et al., 2015c](#)) and three  
244 measurements of a weathered outcrop of the Cretaceous Mancos Shale ([Clark and Johnson,](#)  
245 [2010](#)). These studies indeed found elemental and sulfide-hosted Se to be isotopically depleted  
246 relative to bulk rock values, and that Se associated with recalcitrant organic matter comprised  
247 the dominant host phase, with an isotopic composition similar to that of the bulk rock ([Clark and](#)  
248 [Johnson, 2010](#); [Stüeken et al., 2015c](#)). Other phase-specific concentration measurements ([Kulp](#)  
249 [and Pratt, 2004](#)) have also shown that organic matter is typically the dominant Se host phase in  
250 ancient marine sediments, which suggests that it could mask larger isotopic variability that is  
251 preserved in the  $\text{Se}^0$  and pyrite phases.

252 In contrast to settings with non-quantitative reduction, strongly anoxic and/or restricted  
253 basins with complete reduction of dissolved Se oxyanions will not fractionate Se isotopes during  
254 burial. This causes the underlying marine sediments to approximately record the isotopic  
255 composition of aqueous Se in that basin, allowing black shales deposited in these settings to be  
256 used to infer the Se isotopic composition of overlying waters. This is conceptually analogous to  
257 using strongly euxinic facies characterized by quantitative Mo scavenging to estimate the Mo-  
258 isotopic composition of contemporaneous seawater (*e.g.*, [Gordon et al., 2009](#)). However, in the  
259 case of Se, (a) quantitative reduction is thought to be possible under anoxic – and not strictly  
260 euxinic – conditions ([Oremland et al., 1989](#); [Rue et al., 1997](#)), and (b) the recorded isotopic ratio  
261 may not be representative of the global ocean due to the shorter marine residence time of Se  
262 ( $10^3$ - $10^4$  yr) than Mo ( $>10^5$  yr; [Morford and Emerson, 1999](#)). Black Sea sediments yielded a  
263  $\delta^{82/78}\text{Se}$  composition (avg.  $+0.2 \pm 0.1\text{‰}$ ,  $n = 12$ ; [Mitchell et al., 2012](#)) that is thought to record  
264 quantitative scavenging of aqueous Se from the overlying watermass, whose  $\delta^{82/78}\text{Se}$   
265 composition is therefore not substantially offset from that of the open ocean. However, the  
266 effects of basinal restriction and hydrography on Se isotope signatures remain unexplored in  
267 ancient settings. In the present study, we evaluate these effects using proxies for watermass  
268 exchange with the open ocean.

269

### 270 2.3 Evolution of the global selenium cycle

271 Although modern marine Se cycling involves a large, oxic reservoir of Se oxyanions with  
272 reductive immobilization limited to porewaters or volumetrically-limited anoxic water columns,  
273 this does not describe the operation of the Se cycle in deep time prior to the oxygenation of the  
274 atmosphere and ocean. In Archean sediments deposited before the Great Oxidation Event (GOE),  
275 Se abundances and isotopic fractionations are typically small – likely owing to limited oxidative  
276 weathering and efficient, quantitative oxyanion reduction in strongly anoxic oceans ([Stüeken et  
277 al., 2015b](#)). Notable exceptions occur during transient pulses of oceanic and atmospheric  
278 oxygenation wherein Se was evidently mobilized at higher rates and accumulated to higher  
279 concentrations in mildly oxic surface waters ([Stüeken et al., 2015a](#); [Koehler et al., 2018](#)). The Se  
280 cycle was substantially perturbed by the GOE, with a significant increase in Se abundance in

281 marine sediments and marked isotopic fractionation suggesting non-quantitative reduction in  
282 suboxic shallow waters (Kipp et al., 2017). The hypothesized mid-Proterozoic interval of reduced  
283 atmospheric  $pO_2$  is marked by muted Se abundances and isotopic variability (Stüeken et al.,  
284 2015b), followed by large isotopic excursions associated with the Neoproterozoic “Snowball  
285 Earth” glaciations that are thought to indicate progressive ocean oxygenation (Pogge von  
286 Strandmann et al., 2015). Following their first appearance in the Neoproterozoic, isotopically  
287 depleted marine sediments became more common in the Phanerozoic as well-oxygenated  
288 oceans with a large Se oxyanion reservoir and non-quantitative reduction became established  
289 (Stüeken et al., 2015b).

290 The units considered in the present study were deposited after deep-ocean oxygenation is  
291 thought to have occurred (Dahl et al., 2010; Chen et al., 2015; see review in Qie et al., 2019). This  
292 implies that a sizable Se oxyanion reservoir would have been available in open-marine settings,  
293 with any deviations from this signal likely attributable to local basinal restriction and redox  
294 chemistry rather than global secular changes in the marine oxygen inventory. We used a variety  
295 of major and trace elemental proxies to account for these potential local effects on Se abundance  
296 and isotopic fractionation in a range of black shales deposited in the late Paleozoic.

297

### 298 **3. Materials**

#### 299 3.1 *Late Pennsylvanian: North American Midcontinent Sea*

##### 300 3.1.1 *Paleogeographic context*

301 The samples utilized in this study come from two intervals of deposition on the North  
302 American craton in the late Paleozoic Era. The first interval we consider is the Late Pennsylvanian,  
303 during which time the North American Midcontinent Sea (NAMS) spread across the Laurentian  
304 Craton (Fig. 2A) at times of glacioeustatic highstand (Heckel, 1977, 1994; Algeo and Heckel, 2008).  
305 Marine waters were supplied to the NAMS from oxygen-depleted intermediate depths of the  
306 eastern tropical Panthalassic Ocean (ETPO) (Algeo et al., 2008a, 2008b), which, in combination  
307 with terrestrial freshwater influx from surrounding mountains (indicated by depletion in  
308 carbonate  $\delta^{18}O$  values; Joachimski and Lambert, 2015; Roark et al., 2017; Jimenez et al., 2019),  
309 led to a “superestuarine” circulation pattern in which oxygen-depleted marine waters underlay

310 a reduced-salinity (probably brackish) surface layer (Algeo et al., 2008a, 2008b; Turner et al.,  
311 2019). Thick and laterally extensive organic-rich shales were deposited beneath these anoxic  
312 deep waters and are preserved across much of the midcontinent United States (Heckel, 1977,  
313 1994; Algeo and Heckel, 2008).

314 The NAMS was separated into distinct basins by submarine structural highs, which  
315 prevented exchange of bottom waters (Heckel, 1977). The largest of these was the Mississippi  
316 River Arch, which divided the Midcontinent Shelf from the Illinois Basin (Fig. 2A) (Algeo and  
317 Herrmann, 2018). Spatial variation in sediment geochemistry across the NAMS has been used to  
318 identify lateral gradients in watermass chemistry (Herrmann et al., 2015, 2019) and sources of  
319 detrital siliciclastic material from the Laurentian Craton, Alleghenian Mountains, and Ouachita  
320 Mountains (Turner et al., 2019). The influx of terrigenous material and freshwater from these  
321 regions led to a counter-clockwise gyral surface circulation pattern (Turner et al., 2019), moving  
322 surface waters toward the Panhandle Strait, *i.e.*, the narrow corridor that connected the  
323 southwestern corner of the NAMS to the Midland Basin and Hovey Channel and thence to the  
324 ETPO (Algeo et al., 2008a, 2008b; Fig. 2A).

325

### 326 3.1.2 *Stratigraphic context of drillcores*

327 In this study, we utilized four organic-rich black shale units from three drillcores from the  
328 NAMS (Fig. 2A; Table 1). The Tacket Shale (lateral equivalent of the Hushpuckney Shale; cf. Algeo  
329 and Maynard, 2004; Cruse and Lyons, 2004) was investigated in drillcore C-TW-1 from the  
330 Oklahoma Geological Survey (cf. Cruse and Lyons, 2004; Algeo and Herrmann, 2018). The Stark  
331 and Muncie Creek shales of the Kansas City Group were investigated in the Edmonds #1A core  
332 from the Kansas Geological Survey (cf. Algeo and Maynard, 2004, 2008). The Teutopolis Shale of  
333 the Mattoon Formation (lateral equivalent of the Heebner Shale; cf. Turner et al., 2019) was  
334 investigated in the Englebart core from the Illinois Geological Survey. The Tacket, Stark, and  
335 Muncie Creek shales belong to the Missourian Stage, and the Teutopolis Shale to the Virgilian  
336 Stage of the North American Upper Pennsylvanian.

337 The three study sites represent a gradient in their proximity to marine source waters. The  
338 Tacket Shale was deposited nearest to the influx of marine waters through the Panhandle Strait,

339 whereas the Stark and Muncie Creek shales were deposited toward the center of the  
340 Midcontinent Shelf (see [Algeo et al., 2008a, their figure 5](#)). The Teutopolis Shale was deposited  
341 in the Illinois Basin and so is likely to have experienced different bottom-water conditions due to  
342 lack of deep-water communication between the Illinois Basin and Midcontinent Shelf ([Algeo and](#)  
343 [Herrmann, 2018](#)). This hydrographic separation figures into our interpretation of controls on Se  
344 enrichment and isotopic variability between these units.

345

### 346 3.2 *Late Devonian: North American Seaway*

#### 347 3.2.1 *Paleogeographic context*

348 The second interval considered in this study is the Late Devonian (and earliest  
349 Carboniferous at one locality; see below), when organic-rich black shales were widely deposited  
350 in multiple basins across the North American continent ([Fig. 2B](#)) in what is referred to as the  
351 North American Seaway (NAS) ([Algeo et al., 2007](#)). The basins within the NAS were typically silled  
352 and thus had limited bottom-water exchange with adjacent basins or the open ocean, although  
353 the degree of restriction was variable from basin to basin ([Algeo et al., 2007](#)). This variation in  
354 watermass restriction provides a basis for interpretation of variability in Se abundance levels and  
355 isotopic compositions in the study units.

356 The easternmost of the black shale successions is from the Appalachian Basin. The oldest  
357 strata are found in the northern part of the basin, dating to the Middle Devonian with deposition  
358 of the Esopus and Needmore shales, followed by the Marcellus Group, Hamilton Group, and  
359 Geneseo through Dunkirk shales of early Late Devonian age ([Werne et al., 2002](#); [Sageman et al.,](#)  
360 [2003](#); [Lash, 2017](#)). The central and southern portions of the Appalachian Basin host younger black  
361 shale successions, with deposition commencing in the Late Devonian, including the Ohio and  
362 Sunbury shales in the central Appalachian Basin and the Chattanooga Shale further south ([Algeo](#)  
363 [et al., 2007](#)). To the west, the Illinois Basin hosts Middle and Upper Devonian shales broadly  
364 assigned to the New Albany Shale (or New Albany Group) (*e.g.*, [Lineback, 1970](#)). There, deposition  
365 commenced in the Middle Devonian with the Portwood and lower Blocher members, followed  
366 by the upper Blocher, Selmier, Morgan Trail, Camp Run and Clegg Creek members in the Late  
367 Devonian ([Algeo et al., 2007](#)). Still further west, widespread black shales across the central to

368 southern Midcontinent region are assigned to the Woodford Formation ([Over, 1992, 2002](#)),  
369 which is up to ~200 m thick in places and of Late Devonian age. To the north, uppermost Devonian  
370 and lowermost Carboniferous black shales of the Bakken Formation were deposited in the  
371 Williston Basin of North Dakota, Montana, and southern Alberta, and its lateral equivalent, the  
372 Exshaw Formation, was deposited in the Elk Point Basin of central and northern Alberta.

373

### 374 3.2.2 Stratigraphic context of drillcores

375 In this study, we analyzed black shale samples from eight sites representing multiple  
376 formations in several basins of the NAS ([Table 1](#)). This approach allowed us to evaluate Se  
377 concentrations and isotopic compositions in basins showing varying degrees of watermass  
378 restriction, from relatively weaker restriction along the southern margin of the NAS (*e.g.*,  
379 Oklahoma Basin) to relatively stronger restriction in craton-interior areas (*e.g.*, Illinois and  
380 Williston basins). The large Appalachian Basin, which extended from its silled southern margin in  
381 Tennessee >1000 km northward to the Catskill Delta complex in New York, is known to have  
382 exhibited internal lateral gradients in sediment chemistry and watermass properties ([Algeo et al.,](#)  
383 [2007; Algeo and Tribovillard, 2009](#)). These environmental conditions contributed to development  
384 of pervasive fine-scale (dm-thick) compositional cyclicity throughout this black shale succession.

385 In the northern Appalachian Basin, we analyzed the black shale succession of the Hanover  
386 and Dunkirk Formations in the West Valley core from western New York state (cf. [Sageman et al.,](#)  
387 [2003; Ver Straeten et al., 2011](#)). In the central Appalachian Basin, we analyzed the Cleveland  
388 Member of the Ohio Shale in the OHLO-2 core from northern Ohio and the KEP-3 core from  
389 northern Kentucky (cf. [Jaminski, 1997; Jaminski et al., 1998](#)). In the southern Appalachian Basin,  
390 we sampled the Chattanooga Shale in the Dupont HGS drillcore from northern Tennessee (cf.  
391 [Over et al., 2019](#)). In the Oklahoma Basin, we analyzed the Woodford Formation at three sites:  
392 the Ryan Shale Pit (RSP) and Classen Lake area YMCA (CLY) outcrops in south-central Oklahoma  
393 (cf. [Over, 1992, 2002](#)) and the Amoco A.J. Davis #9 (AJD) drillcore from Yoakum County, Texas. In  
394 the Williston Basin, we sampled the Upper Bakken Shale in the Texaco Thompson #5-1 core from  
395 Billings County, North Dakota (cf. [Hartwell, 1998](#)). We additionally compiled published Se  
396 concentration and isotopic data from the Camp Run member of the New Albany Shale ([Mitchell](#)

397 [et al., 2012](#)). All of the sampled units listed above date to the Late Devonian (Frasnian-Famennian  
398 stages), with the exception of the Upper Bakken Shale, which was deposited in the earliest  
399 Mississippian.

400

#### 401 **4. Methods**

##### 402 4.1 *Selenium measurements*

403 Samples were prepared for Se isotope analysis following published protocols ([Stüeken et al.,](#)  
404 [2013](#)). Homogenized rock powders were dissolved in a mixture of concentrated HF, concentrated  
405 HClO<sub>4</sub>, and 8 M HNO<sub>3</sub> at 130°C. Digests were then evaporated to incipient dryness and additional  
406 HClO<sub>4</sub> was added to ensure complete oxidation of recalcitrant organic matter. The final digests  
407 were evaporated to incipient dryness, 6 M HCl was added, and beakers were placed in a boiling  
408 water bath for at least 30 minutes in order to reduce all Se<sup>VI</sup> to Se<sup>IV</sup>. Solutions were then diluted  
409 to 0.6 M HCl and run through thiol cotton fiber (TCF) columns for separation of Se. Following  
410 column chemistry, Se was liberated from the TCF by adding concentrated HNO<sub>3</sub> to the resin in  
411 test tubes, which were then placed in a boiling water bath for 20 minutes. Selenium was  
412 recovered from the solution in weak HNO<sub>3</sub> via centrifugation. The weak HNO<sub>3</sub> solution was  
413 evaporated down to 0.5 mL at 55°C, at which point aqua regia (3:1 HCl:HNO<sub>3</sub>) was added to the  
414 sample to remove germanium ([Stüeken et al., 2013](#)). The aqua regia solution was also evaporated  
415 down to 0.5 mL, at which point the sample was re-dissolved in 6 M HCl and boiled in a water bath  
416 for 30 minutes to ensure quantitative reduction to Se<sup>IV</sup>. The final sample solution was diluted to  
417 0.6 M HCl for analysis.

418 The measurement of Se concentrations and isotope ratios was conducted on a Nu Plasma  
419 Multicollector Inductively Coupled Plasma Mass Spectrometer (MC-ICP-MS) in the Isotope  
420 Geochemistry Laboratory at University of Washington following analytical protocols described by  
421 [Stüeken et al. \(2013\)](#). Sample solutions were introduced to the MC-ICP-MS via a hydride  
422 generator (HG). Sample solutions were mixed in the HG with a 1% NaBH<sub>4</sub> solution to catalyze the  
423 reduction of Se<sup>IV</sup> to Se<sup>-II</sup> (in the form of H<sub>2</sub>Se), which was then carried across a teflon membrane  
424 and into the MC-ICP-MS via argon (Ar) carrier gas.

425 Lens voltage potentials, position of the plasma torch, and carrier gas flow rate were tuned  
426 daily to optimize signal strength and stability. Measurements were normalized using standard-  
427 sample bracketing with the Se NIST SRM 3149 solution (cf. [Carignan and Wen, 2007](#)) as the  
428 bracketing standard. Isobaric interferences deriving from Ar species were corrected following the  
429 method of [Stüeken et al. \(2013\)](#); other isobaric interferences were negligible within analytical  
430 precision and so were not corrected. All isotopic data are reported in delta notation relative to  
431 NIST reference SRM 3149. We report isotopic data as  $\delta^{82/78}\text{Se}$  values because this isotopic pair is  
432 the least affected by isobaric interferences under our analytical protocol. We note that many  
433 other studies (*e.g.*, [Chang et al., 2017](#); [Mitchell et al., 2012, 2016](#); [Pogge von Strandmann et al.,](#)  
434 [2015](#); [Schilling et al., 2011](#)) report Se isotopic data as  $\delta^{82/76}\text{Se}$  values; these ratios can be  
435 converted to  $\delta^{82/78}\text{Se}$  if it is assumed that Se isotopic fractionation is mass-dependent (cf. [Stüeken](#)  
436 [et al., 2013, 2015b](#); [Pogge von Strandmann et al., 2014](#)).

437 The external reproducibility of  $\delta^{82/78}\text{Se}$  measurements was  $\pm 0.36\text{‰}$  ( $2\sigma$ ), determined by  
438 replicate digestions and analyses ( $n = 11$ ) of in-house standard UW-McRae over a period of six  
439 months. The average internal uncertainty ( $2\text{ SE}$ , *i.e.* 95% confidence interval) of replicate sample  
440 analyses was  $\pm 0.25\text{‰}$ . Samples were analyzed in replicate whenever possible; all isotopic data  
441 are reported with 95% confidence intervals unless stated otherwise. Isotopic data obtained for  
442 in-house standard UW-McRae and USGS standard SGR-1 were  $+0.91 \pm 0.10\text{‰}$  ( $n = 11$ , separate  
443 digests) and  $-0.14 \pm 0.28\text{‰}$  ( $n = 4$ , separate digests), respectively, which are in agreement with  
444 previous studies ([Mitchell et al., 2012](#); [Stüeken et al., 2013, 2015b](#); [Kurzawa et al., 2017](#); [Kipp et](#)  
445 [al., 2017](#); [Pogge von Strandmann et al., 2014, 2015](#); [Schilling et al., 2011](#)). Uncertainty for Se  
446 concentration measurements was  $\pm 7\%$  (RSD).

447

#### 448 4.2 *Published data compilation*

449 Additional major and trace element data were compiled from published studies to  
450 supplement the Se data generated in this study. Where additional data had not been published,  
451 we made measurements following the protocols described below. All data that form the basis of  
452 conclusions drawn in this paper are reported in [Tables 2-4](#) with corresponding references to  
453 original studies in the cases of compiled data.

454

#### 455 4.3 *Organic carbon and nitrogen measurements*

456 The concentration and isotopic composition of total nitrogen and organic carbon were  
457 measured on de-carbonated powders following published protocols (Kipp et al., 2018). Bulk rock  
458 powders were treated with two overnight iterations of 6 M HCl to dissolve all carbonate phases.  
459 De-carbonated powders were then rinsed with 18 MΩ DI-H<sub>2</sub>O and dried in an oven at 60°C. The  
460 dried powders were weighed into tin cups for analysis. Total nitrogen (TN), total organic carbon  
461 (TOC), and the isotopic composition of bulk nitrogen ( $\delta^{15}\text{N}$ ) and organic carbon ( $\delta^{13}\text{C}$ ) were  
462 measured on single aliquots of decarbonated powder on a Costech™ ECS 4010 Elemental Analyzer  
463 coupled to a ThermoFinnigan™ MAT253 continuous flow isotope ratio mass spectrometer housed  
464 in IsoLab at the Department of Earth and Space Sciences, University of Washington. Combustion  
465 was carried out at 1000°C. The sample gases were carried through a reduced copper column to  
466 reduce NO<sub>x</sub> species to N<sub>2</sub> and scrub excess O<sub>2</sub> from the gas stream. A magnesium perchlorate  
467 trap was then used to remove water from the gas stream. Raw data were corrected using a two-  
468 point calibration (Coplen et al., 2006) with three in-house standards: two glutamic acids (GA1,  
469 TOC = 40.8%, TN = 9.5%,  $\delta^{13}\text{C} = -28.3\text{‰}$ ,  $\delta^{15}\text{N} = -4.6\text{‰}$ ; GA2, TOC = 40.8, TN = 9.5,  $\delta^{13}\text{C} = -13.7\text{‰}$ ,  
470  $\delta^{15}\text{N} = -5.7\text{‰}$ ) and dried salmon (SA, TOC = 45.7%, TN = 11.8%,  $\delta^{13}\text{C} = -21.3\text{‰}$ ,  $\delta^{15}\text{N} = +11.3\text{‰}$ ),  
471 which are calibrated to international reference materials USGS-40 and USGS-41 and were  
472 analyzed four times each per analytical session. Isotopic data are reported in delta notation  
473 relative to air for nitrogen and Vienna Pee Dee Belemnite (VPDB) for carbon. Analytical blanks  
474 resulting from combustion were measured and subtracted from nitrogen data; analytical blanks  
475 were below detection limits for carbon. The external reproducibility ( $1\sigma$ ) of isotopic  
476 measurements across all runs, as determined by replicate analyses of in-house standard UW-  
477 McRae ( $\delta^{15}\text{N} = +5.6\text{‰}$ ,  $\delta^{13}\text{C}_{\text{org}} = -37.4\text{‰}$ ), was  $\pm 0.3\text{‰}$  for  $\delta^{15}\text{N}$  and  $\pm 0.1\text{‰}$  for  $\delta^{13}\text{C}$ . Average  
478 precision (RSD) of concentration measurements was  $\pm 2\%$  for TN and  $\pm 0.5\%$  for TOC.

479

#### 480 4.4 *Total sulfur measurements*

481 For total sulfur (TS) analysis, bulk rock powders were weighed into tin cups along with V<sub>2</sub>O<sub>5</sub>  
482 as a combustion aid. Measurements were conducted using a Eurovector Elemental Analyzer

483 coupled to a ThermoFinnigan™ MAT253 continuous flow isotope ratio mass spectrometer housed  
484 in IsoLab at the Department of Earth and Space Sciences, University of Washington. Combustion  
485 was carried out at 1050°C. The combustion products were carried through a magnesium  
486 perchlorate trap to remove oxygen from the gas stream, followed by an 850°C quartz chip column  
487 to allow complete equilibration of oxygen isotopes in the resulting SO<sub>2</sub> with oxygen in the quartz  
488 chips (Fry et al., 2002). Raw data were corrected using a two-point calibration with three in-house  
489 standards: zinc sulfide (ZnS, TS = 32.9%) silver sulfide (Ag<sub>2</sub>S, TS = 12.9%) and barium sulfate  
490 (BaSO<sub>4</sub>, TS = 13.7%), which are calibrated to international reference material IAEA-S-1 and were  
491 analyzed three times each per analytical session. The average precision of TS measurements, as  
492 determined by replicate analyses of in-house standard BaSO<sub>4</sub>, was ±2% (RSD).

493

#### 494 4.5 Statistical analyses

495 Linear and logarithmic regression were used to assess the relationships between various  
496 geochemical data within and among units (see Results). Data binned across the NAMS and NAS  
497 sample sets were compared using the Wilcoxon rank sum tests due to rejection of the null  
498 hypothesis in the Shapiro-Wilk normality test for all parameters.

499

### 500 5. Results

501 All new and compiled data for the Upper Pennsylvanian black shales of the NAMS are  
502 presented in Table 2. Selenium isotope ratios in this dataset range from -1.15‰ to +0.77‰, with  
503 unit averages showing >1‰ variation, *i.e.*, Muncie Creek = +0.50 ± 0.21‰ (*n* = 5), Tackett = -0.01  
504 ± 0.28‰ (*n* = 7), Stark = -0.13 ± 0.38‰ (*n* = 6), and Teutopolis = -0.55 ± 0.25‰ (*n* = 7). Selenium  
505 concentrations range from 0.3 to 135.5 µg/g. Selenium enrichment factors (EF), calculated  
506 following the approach of Tribovillard et al. (2006), and with the same crustal Se/Al ratio (Se/Al  
507 = 17.4 µg/g) that has been used in recent deep-time Se studies (Stüeken et al., 2015a; Koehler et  
508 al., 2018), range from 1.7 to 1465. Across all NAMS samples, δ<sup>82/78</sup>Se values positively correlate  
509 with TOC (wt. %) (*p* < 0.01; *R*<sup>2</sup> = 0.60, linear regression) as well as Se (EF) (*p* < 0.01; *R*<sup>2</sup> = 0.41,  
510 linear regression) (Fig. 3).

511 No statistically significant correlations are observed between unit average  $\delta^{82/78}\text{Se}$  values  
512 and proxies for redox or hydrographic conditions for the four Upper Pennsylvanian study units  
513 (Fig. 3). Nitrogen isotope ratios are nearly invariant (unit means range from +5.5‰ to +7.2‰)  
514 and do not correlate with  $\delta^{82/78}\text{Se}$  values ( $p = 0.89$ ). Fe/Al (g/g) ratios do not correlate with  
515  $\delta^{82/78}\text{Se}$  values ( $p = 0.89$ ) and are similar in all units except the Tacket Shale, which is more Fe-  
516 rich. Similarly,  $\text{DOP}_T$  (the degree of pyritization as estimated from total S and Fe contents; Algeo  
517 et al., 2008b) is highest in the Tacket Shale, and across all units  $\text{DOP}_T$  is not correlated with  
518  $\delta^{82/78}\text{Se}$  values ( $p = 0.78$ ). Moderate differences between units are observed in average Mo/TOC  
519 ratios, which range from ~3 to 10 ( $10^4 \times \text{g/g}$ ), but this variability is not correlated with  $\delta^{82/78}\text{Se}$   
520 values ( $p = 0.55$ ). Mean Sr/Ba ratios of individual units range from 0.5 to 1.0 (g/g) and do not  
521 correlate with  $\delta^{82/78}\text{Se}$  values ( $p = 0.88$ ).

522 In contrast to the lack of relationships with unit average values, individual data points  
523 within certain units show significant correlations between Se concentrations ( $\mu\text{g/g}$ ) and  
524 enrichment factors (EF) and other geochemical proxies. For example, Se concentrations correlate  
525 positively with Mo/TOC ( $p < 0.01$ ,  $R^2 = 0.31$ , logarithmic regression, Fig. 4A) and Se (EF) correlates  
526 positively with Mo (EF) ( $p < 0.01$ ,  $R^2 = 0.62$ , logarithmic regression, Fig. 4B) for the units deposited  
527 on the Midcontinent Shelf (Tacket, Stark, Muncie Creek). Within these units,  $\delta^{82/78}\text{Se}$  values are  
528 also positively correlated with Se ( $\mu\text{g/g}$ ) ( $p < 0.01$ ,  $R^2 = 0.48$ ). Note that this excludes the  
529 Teutopolis Shale, which was deposited in the Illinois Basin (Fig. 4) and thus was isolated from  
530 bottom-water exchange with the Midcontinent Shelf (Algeo and Herrmann, 2018).

531 All new and compiled data from the eight study units of the Late Devonian NAS are  
532 presented in Table 3. Compiled unit average Mo/TOC and Sr/Ba ratios are presented in Table 4.  
533 Selenium isotope ratios in these units range from -1.0‰ to +1.55‰, with unit averages showing  
534 ~1.4‰ variation: Bakken =  $-0.31 \pm 0.50\text{‰}$  ( $n = 4$ ), Woodford =  $-0.18 \pm 0.37\text{‰}$  ( $n = 8$ ), Hanover-  
535 Dunkirk =  $-0.16 \pm 0.28\text{‰}$  ( $n = 4$ ), Ohio Shale (KEP-3 core) =  $-0.16 \pm 0.46\text{‰}$  ( $n = 6$ ), Chattanooga  
536 =  $+0.29 \pm 0.68\text{‰}$  ( $n = 6$ ), New Albany (oxic) =  $+0.45 \pm 0.14\text{‰}$  ( $n = 5$ ), Ohio Shale (OHLO-2 core) =  
537  $+0.69 \pm 0.22\text{‰}$  ( $n = 7$ ), and New Albany (anoxic) =  $+1.14 \pm 0.22\text{‰}$  ( $n = 5$ ) (Fig. 5). Se concentrations  
538 range from 0.3 to 37.0  $\mu\text{g/g}$  (Fig. 5). Unlike in the NAMS shales,  $\delta^{82/78}\text{Se}$  values are only weakly  
539 correlated with TOC/TS ( $p < 0.01$ ,  $R^2 = 0.17$ , logarithmic regression; Fig. 6A). Also unlike the NAMS

540 shales,  $\delta^{82/78}\text{Se}$  values in the NAS samples are negatively correlated with  $\delta^{15}\text{N}$  values ( $p < 0.01$ ,  $R^2$   
541 = 0.30, linear regression; Fig. 6B). Se concentrations are also correlated with  $\delta^{15}\text{N}$  values in the  
542 NAS samples ( $p < 0.01$ ,  $R^2 = 0.47$ , logarithmic regression; Fig. 6C). Unit average  $\delta^{82/78}\text{Se}$  values  
543 show a significant negative correlation with Mo/TOC ( $p = 0.01$ ,  $R^2 = 0.77$ , logarithmic regression)  
544 (Fig. 7) for the NAS samples.

545 Across both datasets as a whole, Se concentrations are significantly higher in the Upper  
546 Pennsylvanian NAMS black shales than those from the Upper Devonian NAS ( $p < 0.01$ ; Fig. 8). The  
547 NAMS shales also have higher Sr/Ba ratios ( $p < 0.01$ ) and  $\delta^{15}\text{N}$  values ( $p < 0.01$ ) than those from  
548 the NAS, but there is no significant difference in TOC ( $p = 0.18$ ) or TS ( $p = 0.48$ ) between the two  
549 datasets (Fig. 8).

550

## 551 6. Discussion

### 552 6.1 Late Pennsylvanian: Potential causes of isotopic variability among units

553 The large range of  $\delta^{82/78}\text{Se}$  values (Fig. 3A) observed in black shales of the NAMS ( $-1.15\%$   
554 to  $+0.77\%$ ) spans much of the range of known Se isotopic variability from the geologic record.  
555 Furthermore, Se enrichment factors in the same samples span nearly 3 orders of magnitude (Fig.  
556 3B). Together these data suggest a diversity of Se cycling regimes across these sites. The most  
557 positive  $\delta^{82/78}\text{Se}$  values co-occur with the largest Se enrichments (Fig. 3A, B), suggesting that a  
558 similar set of mechanisms controlled this covariation.

559 This wide range of Se enrichments and isotopic ratios conceivably could have arisen from  
560 variable redox conditions between the study sites. Specifically, sites with the most reducing  
561 bottom waters might be expected to have scavenged Se most efficiently, thereby leading to large  
562 Se enrichments and positive  $\delta^{82/78}\text{Se}$  values due to quantitative oxyanion reduction. In contrast,  
563 sites with bottom-waters that were suboxic or only transiently anoxic might have experienced  
564 non-quantitative Se reduction, thus yielding smaller Se enrichments and more negative  $\delta^{82/78}\text{Se}$   
565 values. However, we do not see compelling evidence for such redox differences between sites.

566 Bulk-sediment  $\delta^{15}\text{N}$  values are nearly constant across the study sites (Fig. 3F), suggesting  
567 that photic zone redox conditions were roughly similar in the different settings. The fact that  $\delta^{15}\text{N}$   
568 values are positive ( $+4$  to  $+7\%$ ; similar to modern marine sediments, cf. Tesdal et al., 2013)

569 suggests that aerobic nitrogen cycling was occurring and a surface-water nitrate reservoir was  
570 present. As nitrate is reduced to N<sub>2</sub> via denitrification at a redox potential similar to that of Se  
571 oxyanion reduction (Fig. 1), this would seem to suggest that the upper water column was similarly  
572 favorable for Se oxyanion accumulation at each site. We therefore cannot invoke different  
573 surface-water redox conditions as a means to explain the variable Se enrichment and isotopic  
574 fractionation across the NAMS.

575 Bottom-water redox conditions can be evaluated using Fe geochemistry. The similarities in  
576 Fe/Al (Fig. 3G) and DOP<sub>T</sub> (Fig. 3H) across study sites – with the exception of the Tackett Shale,  
577 which has elevated values likely due to local euxinia (Cruse and Lyons, 2004; Algeo and Herrmann,  
578 2018) – suggest that variable bottom-water redox conditions were not responsible for the  
579 observed variations in δ<sup>82/78</sup>Se or Se (EF). All Fe/Al and DOP<sub>T</sub> values are consistent with anoxic  
580 deposition across the NAMS, as inferred in earlier studies (Algeo and Maynard, 2004; Algeo and  
581 Heckel, 2008); however, we note that these Fe data cannot constrain the depth of the  
582 chemocline, which may have been variable across the basin.

583 If redox was not the dominant control on Se enrichment and isotopic fractionation across the  
584 NAMS, another possible mechanism for generating the observed variability in Se cycling is that  
585 basinal restriction influenced the size and isotopic composition of the aqueous Se reservoir. In  
586 modern anoxic, silled basins, rapid removal of redox-sensitive elements to the sediment without  
587 sufficient resupply is known to diminish aqueous Mo concentrations (Algeo and Lyons, 2006),  
588 leading to lower sediment Mo/TOC ratios in more strongly restricted settings. We do observe  
589 some variability in Mo/TOC ratios across our dataset (Fig. 3I), perhaps suggesting varying degrees  
590 of restriction (though this could be confounded by differing degrees of euxinia between sites);  
591 however, these trends do not align with Se isotopes or abundances when viewed across all NAMS  
592 units. We also compiled Sr/Ba ratios from these samples, as this parameter has recently been  
593 proposed as a paleosalinity proxy in shales (Wei et al., 2018; Wei and Algeo, 2019, this issue).  
594 Higher Sr/Ba ratios imply greater seawater influence (due to greater Sr concentrations relative  
595 to Ba, the latter being effectively scavenged by sulfate in estuarine settings), but we do not  
596 observe much variability in Sr/Ba across the study sites. This suggests that variable  
597 seawater/freshwater mixing cannot readily account for the observed changes in Se cycling. Such

598 a correlation may not be expected, though, since the average Se concentration in river waters  
599 (median  $1.1^{+2.2}_{-0.8}$  nM; Conde and Alaejos, 1997) is similar to that of seawater (1-2 nM).

600 The lack of evidence for strong redox and salinity gradients across the NAMS is consistent  
601 with the recent findings of [Algeo and Herrmann \(2018\)](#). Notably, that study identified a large  
602 gradient in redox-sensitive trace metal enrichment across the NAMS, with strong enrichments of  
603 Mo, U and Zn limited to the most proximal areas of the Midcontinent Shelf. They inferred that  
604 this pattern was the result of a nutrient trap akin to that observed in modern estuaries ([Shiller,  
605 1996; Audry et al., 2006](#)). In these settings, nutrients and trace metals dissolved in seawater are  
606 scavenged in the upper portion of the water column by organic matter (derived from primary  
607 production and/or riverine input) and Fe-Mn-oxides (delivered predominantly by rivers). These  
608 organic complexes and particulates sink into bottom waters, where trace metals are then  
609 released through reductive dissolution of the host phases. Because bottom waters flow in the  
610 landward direction in estuarine circulation systems, this mechanism leads to a progressive  
611 concentration of nutrients and trace metals across the most proximal part of the deep  
612 watermass, *i.e.*, the “salt wedge” ([Algeo and Herrmann, 2018](#)). This process can lead to extreme  
613 local enrichments of nutrients and trace metals in sediments. In the case of the NAMS, a sharp  
614 drop in trace-metal enrichments between the Midcontinent Shelf and the Illinois Basin to its east  
615 was interpreted to represent a lack of deep-water exchange between those areas owing to the  
616 physical barrier of the Mississippi River Arch ([Algeo and Herrmann, 2018](#)).

617 Our Se data also seem to be best explained by the nutrient-trap mechanism. Se  
618 concentrations in Midcontinent Shelf samples correlate with Mo/TOC ratios ([Fig. 4A](#)), suggesting  
619 a shared control on the enrichment of these elements. The Teutopolis Shale samples from the  
620 Illinois Basin also show a different trajectory with smaller Se enrichments ([Fig. 4A](#)), consistent  
621 with the isolation of deep waters of the Illinois Basin from the Midcontinent Shelf. The nutrient-  
622 trap mechanism can also account for the observed gradient in  $\delta^{82/78}\text{Se}$  values, with more positive  
623  $\delta^{82/78}\text{Se}$  values occurring in the most trace-metal-enriched samples ([Fig. 4A](#)). One possible  
624 explanation for this trend is that non-quantitative Se sequestration in distal sedimentary pore  
625 waters of the Midcontinent Shelf preferentially drew lighter Se isotopes into the sediments,  
626 enriching the residual aqueous Se reservoir in heavier isotopes, which were then captured via

627 quantitative reduction in the more proximal shelf areas where nutrient trapping was operative.  
628 Quantitative reduction in these proximal areas may have been facilitated by high rates of organic  
629 matter export to sediments. The lighter  $\delta^{82/78}\text{Se}$  values in the Teutopolis Shale are indicative of a  
630 separate deep-water Se reservoir that was not affected by the enrichment process operating in  
631 deep waters of the Midcontinent Shelf.

632 In this scenario of a nutrient-trap control on Se cycling on the Midcontinent Shelf, organic  
633 matter was likely the dominant shuttle for transfer of Se to deep waters. This is indicated by the  
634 similar trajectories of Se (EF) and TOC between study units (Fig. 3B, C). In contrast, Se  
635 enrichments do not correlate with TS (Fig. 3D), suggesting that Se transfer to the sediment was  
636 not controlled by rates of microbial sulfate reduction or pyrite formation. These observations are  
637 notable for two reasons. First, it may help to explain why Se is more strongly enriched than Mo  
638 in the Midcontinent Shelf samples (Fig. 4B). If substantial organic matter recycling was occurring  
639 in the NAMS water column (namely in the more distal portions of the basin), then Se may have  
640 been regenerated more efficiently than Mo, which was likely being recycled predominantly via  
641 Mn-oxide dissolution in sediment porewaters (and thus was prone to some degree of  
642 sequestration via co-precipitation with sulfide minerals). Second, the dominance of total Se by  
643 the organic-bound fraction has important implications for bulk rock Se isotopic compositions. As  
644 described above, enrichment of proximal bottom waters of the Midcontinent Shelf in heavy Se  
645 isotopes could explain the observed trend in  $\delta^{82/78}\text{Se}$  values.

646 An alternative possibility is that Se isotopic variability reflects two-component mixing, in  
647 which the organic-bound  $\text{Se}^{\text{II}}$ , sulfide-bound  $\text{Se}^{\text{II}}$ , and  $\text{Se}^0$  fractions have different  $\delta^{82/78}\text{Se}$   
648 compositions. The limited phase-specific data available suggest that Se can be present in  
649 subequal quantities in organic matter and sulfide minerals (Stüeken et al., 2015c), which is also  
650 supported by Se data from phytoplankton biomass (Mitchell et al., 2012) and sedimentary pyrite  
651 (Large et al., 2014). Given plausible isotopic compositions for the organic and sulfidic components  
652 (e.g.,  $\delta^{82/78}\text{Se}_{\text{organic}} = +0.3\text{‰}$  to  $+1.0\text{‰}$ , ranging from the modern seawater value to a slightly  
653 elevated value assuming isotopic enrichment can be captured by the organic phase, and  
654  $\delta^{82/78}\text{Se}_{\text{sulfide}} = -2.0\text{‰}$  to  $-1.0\text{‰}$ , here for simplicity assuming any  $\text{Se}^0$  has the same isotopic  
655 composition as the sulfide phase, and ranging from the  $\sim -1\text{‰}$  value determined in a phase-

656 specific analysis by [Stüeken et al., 2015c](#) to a lighter value based on their observation that bulk-  
657 rock values got  $\sim 1.5\%$  lighter in that section), it would be possible to generate the range of  
658 observed bulk rock  $\delta^{82/78}\text{Se}$  compositions in the NAMS black shales. In this case, as TOC levels  
659 increase, the organic Se fraction would become dominant over the sulfide and  $\text{Se}^0$  fractions,  
660 leading to higher bulk-rock  $\delta^{82/78}\text{Se}$  values (*i.e.*, approaching that of the organic-bound Se). We  
661 cannot disprove this possibility, but we regard it as secondary to the nutrient-trapping  
662 mechanism. The relationship of Se isotopes ([Fig. 3A](#)) to TOC ([Fig. 3C](#)) is stronger than that of Se  
663 isotopes and TOC/TS ([Fig. 3E](#)). These observations suggest that the organic Se fraction exerted  
664 the dominant influence on the bulk-rock  $\delta^{82/78}\text{Se}$  composition, which is consistent with the  
665 nutrient-trap hypothesis and a progressive enrichment of heavy Se isotopes in the salt wedge  
666 toward the landward portion of the basin. Further phase-specific Se isotope work (cf. [Stüeken et](#)  
667 [al., 2015c](#)) would help to resolve the role of multi-component mixing on bulk rock Se isotopic  
668 variability in the geologic record, particularly if future studies individually characterize the  
669 organic, sulfide and  $\text{Se}^0$  phases.

670

## 671 6.2 *Late Devonian: Effect of watermass restriction on Se isotope ratios*

672 The deposition of black shales in the Late Devonian NAS provides another case study of Se  
673 burial and isotopic fractionation in basins with variable redox and hydrographic conditions ([Algeo](#)  
674 [et al., 2007](#)). As in the Late Pennsylvanian NAMS, considerable Se isotopic variability is observed  
675 between units, with  $\delta^{82/78}\text{Se}$  values spanning much of the range observed in the geologic record.  
676 As in the NAMS dataset, the  $\delta^{82/78}\text{Se}$  of NAS black shales correlates only weakly with TOC/TS ratios  
677 ([Fig. 6A](#)), suggesting that variable mixing of organic- and sulfide-bound Se fractions is not the  
678 dominant control on bulk-rock  $\delta^{82/78}\text{Se}$  compositions.

679 For the NAS dataset,  $\delta^{82/78}\text{Se}$  shows significant negative covariation with  $\delta^{15}\text{N}$  ([Fig. 6B](#)). One  
680 possible explanation for this relationship is that watermasses with near-zero  $\delta^{15}\text{N}$  values – which  
681 reflect systems with scarce nitrate and dominated by nitrogen fixation ([Ader et al., 2016](#); [Stüeken](#)  
682 [et al., 2016](#)) – are also depleted in Se oxyanions, since Se reduction is initiated at redox potentials  
683 similar to denitrification ([Fig. 1](#)). This scenario may be typical of more restricted settings in which  
684 nitrate is not readily replenished from a seawater source. Over time, such basins would tend to

685 deplete their nitrate reservoirs, leading to strong nitrogen fixation as observed in the modern  
686 Black Sea (Fulton et al., 2012). A concurrent depletion of Se oxyanions would result in progressive  
687 enrichment of heavy isotopes in the residual aqueous Se reservoir (it is important to note that  
688 the Se cycle has no equivalent to N<sub>2</sub> fixation, *i.e.*, there is no source of isotopically light Se upon  
689 depletion of the Se oxyanion reservoir.) This inference is supported by the positive correlation  
690 between Se concentrations and  $\delta^{15}\text{N}$  values in the NAS black shales (Fig. 6C). Units with near-zero  
691  $\delta^{15}\text{N}$  values indicative of a limited aqueous nitrate reservoir also tend to have low Se contents  
692 ( $\sim 1$   $\mu\text{g/g}$  or less). The only samples with Se concentrations  $>10$  ppm also have  $\delta^{15}\text{N}$  close to that  
693 of modern seawater nitrate ( $\sim +5\text{‰}$ ), which is consistent with a close linkage between N and Se  
694 cycling. As bottom water redox conditions were more-or-less uniformly anoxic across all of the  
695 NAS basins (Algeo et al., 2007), we infer that differences in  $\delta^{82/78}\text{Se}$  between study units in  
696 different basins were due to variable degrees of basinal restriction and seawater renewal times.

697 Another way to test this hypothesis is to look for evidence of basinal restriction in other  
698 geochemical proxies. Basinal restriction commonly results in development of non-marine  
699 salinities, and paleosalinity variation in shale facies can be inferred from Sr/Ba ratios (Wei et al.,  
700 2018; Wei and Algeo, 2019, this issue). Across the NAS units sampled here, average Sr/Ba ratios  
701 range from 0.16 to 0.45 (Fig. 5; Table 4), which is consistent with mostly brackish (0.2-0.5) rather  
702 than marine salinity conditions ( $>0.5$ , as defined by Wei and Algeo, 2019, this issue). Thus, all of  
703 the interior NAS basins show a degree of watermass restriction, promoting mixing of seawater  
704 with freshwater runoff from the Laurentian Craton. However, unit-average Sr/Ba does not  
705 correlate strongly with  $\delta^{82/78}\text{Se}$  ( $R^2 = 0.07$ ), perhaps because salinity and seawater renewal times  
706 are not strongly coupled in restricted-basinal settings (cf. Algeo and Lyons, 2006). Mo/TOC ratios  
707 can also reflect the degree of basinal restriction if bottom-water redox conditions are uniform  
708 (Algeo and Lyons, 2006), which is approximately true of NAS black shales (Algeo et al., 2007; note  
709 that the bioturbated gray shale horizons of the New Albany Shale were excluded from this  
710 analysis because bioturbation implies at least transiently oxic conditions). In contrast to Sr/Ba,  
711 unit-average Mo/TOC exhibits a strong negative correlation with  $\delta^{82/78}\text{Se}$  (Fig. 7), which may  
712 indicate a hydrographic control on  $\delta^{82/78}\text{Se}$  in the NAS. Specifically, more restricted basins in  
713 which aqueous Mo is strongly depleted also tend to become more enriched in heavy Se isotopes

714 as their Se reservoir is drawn down. We note that the  $\delta^{82/78}\text{Se}$  vs. Mo/TOC relationship is based  
715 on relatively few data (6 units), but it is supported by the Se- $\delta^{15}\text{N}$  relationships discussed above  
716 and by Sr/Ba evidence of generally brackish conditions, all of which are consistent with basinal  
717 restriction imparting a strong influence on Se isotopic compositions in the Late Devonian NAS.

718 The implication for controls on  $\delta^{82/78}\text{Se}$  compositions is that deep-water renewal in less  
719 restricted basins can replenish Se oxyanions, providing a larger Se reservoir that is less prone to  
720 quantitative reduction. This process can account for lower  $\delta^{82/78}\text{Se}$  in the Woodford Shale of the  
721 relatively open Oklahoma Basin relative to the more-restricted Appalachian and Illinois basin  
722 black shales. These data demonstrate the influence of basin hydrography on  $\delta^{82/78}\text{Se}$  values in  
723 reducing marine sediments, as previously inferred based on more limited evidence (Stüeken et  
724 al., 2015b). The implication for the use of  $\delta^{82/78}\text{Se}$  values as a paleo-redox proxy is that strongly  
725 restricted basins may not record signals that are representative of Se cycling in the open ocean.  
726 The marked enrichment of heavy Se isotopes in anoxic horizons of the New Albany Shale provides  
727 no evidence of non-quantitative oxyanion reduction, which could be interpreted as evidence of  
728 an anoxic deep ocean. However, the Woodford Shale, which was accumulating at the same time  
729 and in closer proximity to the open ocean (and with a shorter renewal time, as inferred from the  
730 higher Mo/TOC ratios; Fig. 5; Algeo et al., 2007), recorded modern-seawater-like  $\delta^{82/78}\text{Se}$  values,  
731 which may be more representative of global Se cycling during the late Devonian. We therefore  
732 recommend that, when employing the Se isotope proxy in deep time, complementary datasets  
733 such as  $\delta^{15}\text{N}$ , Sr/Ba and Mo/TOC be generated and evaluated across differing formations of  
734 similar age and setting. Although each paleoenvironmental proxy faces its own limitations, a  
735 combined approach allows the strongest possible inferences about ancient watermass chemistry.  
736 This will be particularly important for application of Se isotopes in the Precambrian, where  
737 comparatively little is known about the paleogeographic context of black shale basins.

738

### 739 6.3 *Comparing controls on Se in Upper Pennsylvanian and Upper Devonian black shales*

740 We close by comparing and contrasting the dominant controls on Se enrichment and  
741 isotopic fractionation between shales deposited in the Late Pennsylvanian NAMS and the Late  
742 Devonian NAS. The most pronounced difference between these two ancient seaways is that Se

743 concentrations reach far higher levels in the NAMS (particularly on the Midcontinent Shelf) than  
744 in any of the Late Devonian NAS basins (Fig. 8). Several factors are likely to have contributed to  
745 this difference.

746 First, as noted in Section 6.2, the Late Devonian NAS basins appear to have been more  
747 restricted (as evidenced by lower Sr/Ba ratios; Fig. 8) than the Midcontinent Shelf and Illinois  
748 Basin in the Late Pennsylvanian. Due to slower seawater renewal times, the waters overlying the  
749 NAS shales became depleted in nitrate (as evidenced by lower  $\delta^{15}\text{N}$  values) and likely also Se  
750 oxyanions (as evidenced by lower Se enrichment; Fig. 8). Importantly, these differences do not  
751 correspond to variations in TOC or TS content (Fig. 8), suggesting that the capacity for Se  
752 enrichment was limited in the NAS basins despite similarly anoxic bottom water conditions and  
753 a similar capacity for shuttling trace metals to deep waters. These considerations highlight the  
754 importance of basinal hydrography in controlling the degree of Se enrichment in restricted  
755 marine basins.

756 Second, the processes by which Se became enriched in the sediment differed between  
757 the Late Pennsylvanian and Late Devonian seaways. As described in Section 6.1, Se enrichment  
758 on the Midcontinent Shelf of the NAMS was likely due to a nutrient-trapping mechanism linked  
759 to its quasi-estuarine circulation pattern (Algeo et al., 2008a, 2008b; Algeo and Herrmann, 2018).  
760 These conditions not only promoted strong Se uptake by the sediment but also led to significantly  
761 greater Se enrichment relative to other redox-sensitive trace metals, including Mo, U and V (Fig.  
762 9). This pattern was probably due to Se being shuttled to deep waters mainly via sinking organic  
763 matter, which was more efficiently recycled in the water column than the Fe-Mn-oxides that  
764 transported trace metals such as Mo to the sediment-water interface. In contrast, the Late  
765 Devonian NAS basins, which were not characterized by the same sort of nutrient trap, show Se  
766 enrichments that are on par with other redox-sensitive trace metals such as U and V (Fig. 9B, C),  
767 and Mo is actually more enriched than Se in some Upper Devonian shales (Fig. 9A). As noted in  
768 Section 6.2, depletion of the Se oxyanion reservoirs in the more restricted NAS basins occurred  
769 alongside nitrate depletion, but to a lesser degree than Mo depletion. This suggests that Se was  
770 being reductively immobilized at relatively high redox potentials, similar to nitrate reduction but  
771 above the redox potential at which Mo is efficiently scavenged (cf. Helz et al., 1996), impeding

772 quantitative removal of aqueous Mo to the sediment. Thus, including Se in paleo-redox studies  
773 can provide additional insights into water column redox thresholds by adding a high-redox-  
774 potential species to the arsenal of trace-metal-enrichment proxies (cf. [Tribovillard et al., 2006](#)).

775 An important implication of both datasets is that bulk-rock  $\delta^{82/78}\text{Se}$  values in restricted  
776 basins can substantially diverge from open-ocean signatures. For deep-time applications of the  
777  $\delta^{82/78}\text{Se}$  proxy, it is therefore imperative to constrain the degree of open-ocean exchange when  
778 interpreting  $\delta^{82/78}\text{Se}$  data in the context of global redox evolution. In the present study, we found  
779 that combining  $\delta^{82/78}\text{Se}$  data with proxies for basinal restriction (Sr/Ba, Mo/TOC) and redox  
780 chemistry ( $\delta^{15}\text{N}$ , Fe/Al, DOP) provided a useful context for evaluating the significance of Se  
781 isotopic variations. Such an integrated approach will be critical in order to make the most  
782 effective use of  $\delta^{82/78}\text{Se}$  as a proxy for Earth's secular oxygenation history.

783

## 784 **7. Conclusions**

785 We have analyzed Se concentrations and isotope ratios in a range of black shales deposited  
786 in epicontinental seas in the late Paleozoic. When viewed within the context provided by other  
787 major and trace elemental data, the Se data seem to reflect differences in both local redox  
788 conditions and basinal hydrography. On the Midcontinent Shelf of the Late Pennsylvanian NAMS,  
789 a quasi-estuarine nutrient trap concentrated Se and other trace metals in saline deep waters that  
790 became progressively isotopically enriched through successive recycling of organic-bound Se. In  
791 contrast, isotopic variability among basins in the Late Devonian NAS appears to have been  
792 controlled by differing hydrographic conditions, where more restricted settings featured Se  
793 oxyanion reduction alongside nitrate reduction with limited re-supply from the open marine  
794 reservoir. This caused the more restricted basins to display lower Se abundances and stronger  
795 isotopic enrichment, in contrast to settings that received greater seawater influx. In both the  
796 NAMS and NAS datasets, the additional context provided by TOC, TS, Mo/TOC, Sr/Ba, Fe/Al, DOP,  
797 and  $\delta^{15}\text{N}$  greatly helped in resolving the environmental drivers of variability in Se abundance and  
798 isotopic composition, although we also note that the dominant biogeochemical controls on the  
799 Se cycle are not captured by any one of those proxies alone. Extending these findings to other  
800 paleo-environmental settings, our results suggest that restricted basins are prone to record

801 enrichment of heavy Se isotopes if not regularly replenished with a seawater source of Se  
802 oxyanions, which can make these settings unsuitable for assessing global redox conditions. The  
803 future utilization of Se isotopes as a paleo-redox proxy will greatly benefit from a concerted effort  
804 to make high-precision, phase-specific measurements, as well as from the use of complementary  
805 datasets to resolve aspects of basinal redox and hydrography that can provide critical context for  
806 Se isotopic interpretations.

807

## 808 **8. Acknowledgments**

809 We thank Scott Kuehner, Fang-Zhen Teng, Bruce Nelson, Yan Hu and Andy Schauer for technical  
810 support. This work was supported by an NSF Graduate Research Fellowship to MAK (DGE-  
811 1256082) and a NASA Exobiology grant to RB (NNX16AI37G). TJA thanks the state geological  
812 surveys of Ohio, Kentucky, Tennessee, New York, Illinois, Kansas, Oklahoma, and North Dakota  
813 for providing access to cores sampled for studies of Upper Pennsylvanian and Upper Devonian  
814 black shales, and Jeff Over for providing samples from three locales of the Woodford Formation.  
815 Three anonymous reviewers are thanked for comments that substantively improved this  
816 manuscript.

817 **References**

818

819 Ader M., Thomazo C., Sansjofre P., Busigny V., Papineau D., Laffont R., Cartigny P. and  
820 Halverson G. P. (2016) Interpretation of the nitrogen isotopic composition of  
821 Precambrian sedimentary rocks: Assumptions and perspectives. *Chem. Geol.* **429**, 93–  
822 110.

823 Algeo T. J. and Heckel P. H. (2008) The Late Pennsylvanian midcontinent sea of North America: a  
824 review. *Palaeogeogr. Palaeoclimatol. Palaeoecol.* **268**, 205–221.

825 Algeo T. J. and Herrmann A. D. (2018) An ancient estuarine-circulation nutrient trap: The Late  
826 Pennsylvanian Midcontinent Sea of North America. *Geology* **46**, 143–146.

827 Algeo T. J. and Lyons T. W. (2006) Mo–total organic carbon covariation in modern anoxic  
828 marine environments: Implications for analysis of paleoredox and paleohydrographic  
829 conditions. *Paleoceanography* **21**.

830 Algeo T. J. and Maynard J. B. (2004) Trace-element behavior and redox facies in core shales of  
831 Upper Pennsylvanian Kansas-type cyclothems. *Chem. Geol.* **206**, 289–318.

832 Algeo T. J. and Maynard J. B. (2008) Trace-metal covariation as a guide to water-mass  
833 conditions in ancient anoxic marine environments. *Geosphere* **4**, 872–887.

834 Algeo T. J. and Tribovillard N. (2009) Environmental analysis of paleoceanographic systems  
835 based on molybdenum–uranium covariation. *Chem. Geol.* **268**, 211–225.

836 Algeo T. J., Lyons T. W., Blakey R. C. and Over D. J. (2007) Hydrographic conditions of the  
837 Devonian–Carboniferous North American Seaway inferred from sedimentary Mo–TOC  
838 relationships. *Palaeogeogr. Palaeoclimatol. Palaeoecol.* **256**, 204–230.

839 Algeo T. J., Heckel P. H., Maynard J. B., Blakey R., Rowe H., Pratt B. R. and Holmden C. (2008a)  
840 Modern and ancient epeiric seas and the super-estuarine circulation model of marine  
841 anoxia. *Dyn. Epeiric Seas Sedimentol. Paleontol. Geochem. Perspect. St Johns Can. Geol.*  
842 *Assoc. Can. Spec. Publ.* **48**, 7–38.

843 Algeo T. J., Rowe H., Hower J. C., Schwark L., Herrmann A. and Heckel P. H. (2008b) Oceanic  
844 denitrification during Late Carboniferous glacial-interglacial cycles. *Nat. Geosci.* **1**, 709–  
845 714.

846 Algeo T. J., Morford J. and Cruse A. (2012) New applications of trace metals as proxies in marine  
847 paleoenvironments. *Chem. Geol.* **306–307**, 160–164.

848 Anbar A. D. and Gordon G. W. (2008) Redox renaissance. *Geology* **36**(3), 271–272.

849

- 850 Anderson R. F., Sachs J. P., Fleisher M. Q., Allen K. A., Yu J., Koutavas A. and Jaccard S. L. (2019).  
851 Deep-Sea Oxygen Depletion and Ocean Carbon Sequestration During the Last Ice Age.  
852 *Global Biogeochem. Cy.* **33**, 301-317.
- 853  
854 Arnold G. L., Anbar A. D., Barling J. and Lyons T. W. (2004) Molybdenum isotope evidence for  
855 widespread anoxia in mid-proterozoic oceans. *Science* **304**, 87–90.
- 856 Audry S., Blanc G., Schäfer J., Chaillou G. and Robert S. (2006) Early diagenesis of trace metals  
857 (Cd, Cu, Co, Ni, U, Mo, and V) in the freshwater reaches of a macrotidal estuary.  
858 *Geochim. Cosmochim. Acta* **70**, 2264–2282.
- 859 Balistrieri L. S. and Chao T. T. (1990) Adsorption of selenium by amorphous iron oxyhydroxide  
860 and manganese dioxide. *Geochim. Cosmochim. Acta* **54**, 739–751.
- 861 Basu A., Schilling K., Brown S. T., Johnson T. M., Christensen J. N., Hartmann M., Reimus P. W.,  
862 Heikoop J. M., Woldegabriel G. and DePaolo D. J. (2016). Se Isotopes as Groundwater  
863 Redox Indicators: Detecting Natural Attenuation of Se and in Situ Recovery U Mine.  
864 *Environ. Sci. Technol.* **50**, 10833-10842.
- 865  
866 Broecker W. S. and Peng T.-H. (1982) *Tracers in the Sea*, Lamont-Doherty Geological  
867 Observatory, Columbia University.
- 868 Brumsack H.-J. (2006) The trace metal content of recent organic carbon-rich sediments:  
869 implications for Cretaceous black shale formation. *Palaeogeogr. Palaeoclimatol.*  
870 *Palaeoecol.* **232**, 344–361.
- 871 Calvert S. E., Bustin R. M. and Ingall E. D. (1996) Influence of water column anoxia and sediment  
872 supply on the burial and preservation of organic carbon in marine shales. *Geochim.*  
873 *Cosmochim. Acta* **60**, 1577–1593.
- 874 Carignan J. and Wen H. (2007) Scaling NIST SRM 3149 for Se isotope analysis and isotopic  
875 variations of natural samples. *Chem. Geol.* **242**, 347–350.
- 876 Chang Y., Zhang J., Qu J.-Q. and Xue Y. (2017) Precise selenium isotope measurement in  
877 seawater by carbon-containing hydride generation-Desolvation-MC-ICP-MS after thiol  
878 resin preconcentration. *Chem. Geol.* **471**, 65–73.
- 879 Chau Y. K. and Riley J. P. (1965). The determination of selenium in sea water, silicates and  
880 marine organisms. *Anal. Chim. Acta.* **33**, 36-49.
- 881  
882 Chen X., Ling H.-F., Vance D., Shields-Zhou G. A., Zhu M., Poulton S. W., Och L. M., Jiang S.-Y., Li  
883 D. and Cremonese L. (2015) Rise to modern levels of ocean oxygenation coincided with  
884 the Cambrian radiation of animals. *Nat. Commun.* **6**, 7142.

- 885 Clark S. K. and Johnson T. M. (2010) Selenium stable isotope investigation into selenium  
886 biogeochemical cycling in a lacustrine environment: Sweitzer Lake, Colorado. *J. Environ.*  
887 *Qual.* **39**, 2200–2210.
- 888 Clarkson M. O., Stirling C. H., Jenkyns H. C., Dickson A. J., Porcelli D., Moy C. M., von  
889 Strandmann P. A. P., Cooke I. R. and Lenton T. M. (2018) Uranium isotope evidence for  
890 two episodes of deoxygenation during Oceanic Anoxic Event 2. *Proc. Natl. Acad. Sci.*  
891 *(U.S.A.)*, 201715278.
- 892 Conde J. E. and Alaejos M. S. (1997). Selenium concentrations in natural and environmental  
893 waters. *Chem. Rev.* **97**, 1979-2004.
- 894
- 895 Coplen T. B., Brand W. A., Gehre M., Gröning M., Meijer H. A., Toman B. and Verkouteren R. M.  
896 (2006) New guidelines for  $\delta^{13}\text{C}$  measurements. *Anal. Chem.* **78**, 2439–2441.
- 897 Cruse A. M. and Lyons T. W. (2004) Trace metal records of regional paleoenvironmental  
898 variability in Pennsylvanian (Upper Carboniferous) black shales. *Chem. Geol.* **206**, 319–  
899 345.
- 900 Cutter G. A. and Bruland K. W. (1984) The marine biogeochemistry of selenium: A re-evaluation.  
901 *Limnol. Oceanogr.* **29**, 1179–1192.
- 902 Dahl T. W., Hammarlund E. U., Anbar A. D., Bond D. P. G., Gill B. C., Gordon G. W., Knoll A. H.,  
903 Nielsen A. T., Schovsbo N. H. and Canfield D. E. (2010) Devonian rise in atmospheric  
904 oxygen correlated to the radiations of terrestrial plants and large predatory fish. *Proc.*  
905 *Natl. Acad. Sci. (U.S.A.)* **107**, 17911–17915.
- 906 Ellis A. S., Johnson T. M., Herbel M. J. and Bullen T. D. (2003). Stable isotope fractionation of  
907 selenium by natural microbial consortia. *Chem. Geol.* **195**, 119-129.
- 908
- 909 Fan H., Wen H., Hu R. and Zhao H. (2011) Selenium speciation in Lower Cambrian Se-enriched  
910 strata in South China and its geological implications. *Geochim. Cosmochim. Acta* **75**,  
911 7725–7740.
- 912 Floor G. H. and Román-Ross G. (2012). Selenium in volcanic environments: A review. *Appl.*  
913 *Geochem.* **27**, 517-531.
- 914
- 915 Fry B., Silva S. R., Kendall C. and Anderson R. K. (2002) Oxygen isotope corrections for online  
916  $\delta^{34}\text{S}$  analysis. *Rapid Commun. Mass Spectrom.* **16**, 854–858.
- 917 Fulton J. M., Arthur M. A. and Freeman K. H. (2012) Black Sea nitrogen cycling and the  
918 preservation of phytoplankton  $\delta^{15}\text{N}$  signals during the Holocene. *Glob. Biogeochem.*  
919 *Cycles* **26**.
- 920 Gordon G. W., Lyons T. W., Arnold G. L., Roe J., Sageman B. B. and Anbar A. D. (2009). When do  
921 black shales tell molybdenum isotope tales? *Geology.* **37**, 535-538.

- 922  
923 Hartwell W. J. (1998) Geochemical and petrographic analysis of the Upper Devonian-Lower  
924 Mississippian Bakken black shales from the Williston Basin, North Dakota. Master's  
925 Thesis, University of Cincinnati, Cincinnati, Ohio.
- 926 Heckel P. H. (1977) Origin of phosphatic black shale facies in Pennsylvanian cyclothems of mid-  
927 continent North America. *AAPG Bull.* **61**, 1045–1068.
- 928 Heckel P. H. (1994) Evaluation of evidence for glacio-eustatic control over marine Pennsylvanian  
929 cyclothems in North America and consideration of possible tectonic effects. In:  
930 Dennison, J.M., Etensohn, F.R. (Eds.), *Tectonic and Eustatic Controls on Sedimentary*  
931 *Cycles*. SEPM, Concepts in Sedimentology and Paleontology 4, pp. 65-87.
- 932 Helz G.R., Miller C.V., Charnock J.M., Mosselmans J.L.W., Pattrick R.A.D., Garner C.D. and  
933 Vaughan D.J. (1996) Mechanisms of molybdenum removal from the sea and its  
934 concentration in black shales: EXAFS evidences. *Geochim. Cosmochim. Acta* **60**, 3631-  
935 3642.
- 936 Herrmann A. D., Barrick J. E. and Algeo T. J. (2015) The relationship of conodont biofacies to  
937 spatially variable watermass properties in the Late Pennsylvanian Midcontinent Sea.  
938 *Paleoceanography* **30**(3), 269-283.
- 939 Herrmann A. D., Barrick J. E., Algeo T. J. and Peng Y. B. (2019) Conodont biofacies and  
940 watermass structure of the Middle Pennsylvanian North American Midcontinent  
941 Sea. *Palaeogeogr. Palaeoclimatol. Palaeoecol.*,  
942 <https://doi.org/10.1016/j.palaeo.2019.109235>.
- 943  
944 Ingall E. D., Bustin R. M. and Van Cappellen P. (1993) Influence of water column anoxia on the  
945 burial and preservation of carbon and phosphorus in marine shales. *Geochim.*  
946 *Cosmochim. Acta* **57**, 303–316.
- 947 Jaminski J. (1997) Geochemical and petrographic patterns of cyclicity in the Devonian-  
948 Mississippian black shales of the Central Appalachian Basin. Ph. D. dissertation,  
949 University of Cincinnati, Cincinnati, Ohio.
- 950 Jaminski J., Algeo T. J., Maynard J. B. and Hower J. C. (1998) Climatic origin of dm-scale  
951 compositional cyclicity in the Cleveland Member of the Ohio Shale (Upper Devonian),  
952 Central Appalachian Basin, USA. In: Schieber J., Zimmerle W. and Sethi P. S., eds., *Shales*  
953 *and Mudstones*, v. 1: Stuttgart, Schweizerbart'sche, pp. 217-242.
- 954 Jimenez M. Y., Ivany L. C., Judd E. J. and Henkes G. (2019) Low and seasonally variable salinity in  
955 the Pennsylvanian equatorial Appalachian Basin. *Earth Planet. Sci. Lett.* **519**, 182–191.

- 956 Joachimski M. M. and Lambert L. L. (2015) Salinity contrast in the US Midcontinent Sea during  
957 Pennsylvanian glacio-eustatic highstands: Evidence from conodont apatite  $\delta^{18}\text{O}$ .  
958 *Palaeogeogr. Palaeoclimatol. Palaeoecol.* **433**, 71–80.
- 959 Johnson T. M. and Bullen T. D. (2003). Selenium isotope fractionation during reduction by Fe(II)-  
960 Fe(III) hydroxide-sulfate (green rust). *Geochim. Cosmochim. Acta.* **67**, 413-419.  
961
- 962 Johnson T. M. and Bullen T. D. (2004) Mass-dependent fractionation of selenium and chromium  
963 isotopes in low-temperature environments. *Rev. Mineral. Geochem.* **55**, 289–317.
- 964 Johnson T. M., Herbel M. J., Bullen T. D. and Zawislanski P. T. (1999) Selenium isotope ratios as  
965 indicators of selenium sources and oxyanion reduction. *Geochim. Cosmochim. Acta* **63**,  
966 2775–2783.
- 967 Kendall B., Dahl T. W. and Anbar A. D. (2017) The stable isotope geochemistry of molybdenum.  
968 *Rev. Mineral. Geochem.* **82**, 683–732.
- 969 Kendall B., Gordon G. W., Poulton S. W. and Anbar A. D. (2011) Molybdenum isotope  
970 constraints on the extent of late Paleoproterozoic ocean euxinia. *Earth Planet. Sci. Lett.*  
971 **307**, 450–460.
- 972 Kendall B., Komiya T., Lyons T. W., Bates S. M., Gordon G. W., Romaniello S. J., Jiang G., Creaser  
973 R. A., Xiao S., McFadden K., Sawaki Y., Tahata M., Shu D., Han J., Li Y., Chu X. and Anbar  
974 A. D. (2015) Uranium and molybdenum isotope evidence for an episode of widespread  
975 ocean oxygenation during the late Ediacaran Period. *Geochim. Cosmochim. Acta* **156**,  
976 173–193.
- 977 Kipp M. A., Stüeken E. E., Bekker A. and Buick R. (2017) Selenium isotopes record extensive  
978 marine suboxia during the Great Oxidation Event. *Proc. Natl. Acad. Sci. (U.S.A.)* **114**,  
979 875–880.
- 980 Kipp M. A., Stüeken E. E., Yun M., Bekker A. and Buick R. (2018) Pervasive aerobic nitrogen  
981 cycling in the surface ocean across the Paleoproterozoic Era. *Earth Planet. Sci. Lett.* **500**,  
982 117–126.
- 983 Koehler M. C., Buick R., Kipp M. A., Stüeken E. E. and Zaloumis J. (2018) Transient surface ocean  
984 oxygenation recorded in the ~2.66 Ga Jeerinah Formation, Australia. *Proc. Natl. Acad.*  
985 *Sci. (U.S.A.)* **115**, 7711–7716.
- 986 Kulp T. R. and Pratt L. M. (2004) Speciation and weathering of selenium in Upper Cretaceous  
987 chalk and shale from South Dakota and Wyoming, USA. *Geochim. Cosmochim. Acta* **68**,  
988 3687–3701.
- 989 Kurzawa T., König S., Labidi J., Yierpan A. and Schoenberg R. (2017) A method for Se isotope  
990 analysis of low ng-level geological samples via double spike and hydride generation MC-  
991 ICP-MS. *Chem. Geol.* **466**, 219–228.

- 992 Large R. R., Halpin J. A., Danyushevsky L. V., Maslennikov V. V., Bull S. W., Long J. A., Gregory D.  
993 D., Lounejeva E., Lyons T. W. and Sack P. J. (2014) Trace element content of sedimentary  
994 pyrite as a new proxy for deep-time ocean–atmosphere evolution. *Earth Planet. Sci.*  
995 *Lett.* **389**, 209–220.
- 996 Lash G. G. (2017) A multiproxy analysis of the Frasnian-Famennian transition in western New  
997 York State, U.S.A. *Palaeogeogr. Palaeoclimatol. Palaeoecol.* **473**, 108–122.
- 998 Lau K. V., Macdonald F. A., Maher K. and Payne J. L. (2017) Uranium isotope evidence for  
999 temporary ocean oxygenation in the aftermath of the Sturtian Snowball Earth. *Earth*  
1000 *Planet. Sci. Lett.* **458**, 282–292.
- 1001 Lau K. V., Maher K., Altiner D., Kelley B. M., Kump L. R., Lehrmann D. J., Silva-Tamayo J. C.,  
1002 Weaver K. L., Yu M. and Payne J. L. (2016) Marine anoxia and delayed Earth system  
1003 recovery after the end-Permian extinction. *Proc. Natl. Acad. Sci. (U.S.A.)* **113**, 2360–  
1004 2365.
- 1005 Lineback J. A. (1970) *Stratigraphy of the New Albany Shale in Indiana*, State of Indiana,  
1006 Department of Natural Resources.
- 1007 Little S. H., Vance D., Lyons T. W. and McManus J. (2015). Controls on trace metal authigenic  
1008 enrichment in reducing sediments: Insights from modern oxygen-deficient settings. *Am.*  
1009 *J. Sci.* **315**, 77–119.
- 1010 Lu W., Ridgwell A., Thomas E., Hardisty D. S., Luo G., Algeo T. J., Saltzman M. R., Gill B. C., Shen  
1011 Y., Ling H.-F., Edwards C. T., Whalen M. T., Zhou X., Gutchess K. M., Jin L., Rickaby R. E.  
1012 M., Jenkyns H. C., Lyons T. W., Lenton T. M., Kump L. R., and Lu Z. (2018) Late inception  
1013 of a resiliently oxygenated upper ocean. *Science* **361**, 174–177.
- 1014 Lu Z., Jenkyns H. C. and Rickaby R. E. M. (2010) Iodine to calcium ratios in marine carbonate as a  
1015 paleo-redox proxy during oceanic anoxic events. *Geology* **38**, 1107–1110.
- 1016 Lyons T. W., Reinhard C. T. and Planavsky N. J. (2014). The rise of oxygen in Earth's early ocean  
1017 and atmosphere. *Nature* **506**, 307–315.  
1018
- 1019 Martens D. A. and Suarez D. L. (1997) Selenium speciation of marine shales, alluvial soils, and  
1020 evaporation basin soils of California. *J. Environ. Qual.* **26**, 424–432.
- 1021 Measures C. I. and Burton J. D. (1980) The vertical distribution and oxidation states of dissolved  
1022 selenium in the northeast Atlantic Ocean and their relationship to biological processes.  
1023 *Earth Planet. Sci. Lett.* **46**, 385–396.
- 1024 Measures C. I., McDuff R. E. and Edmond J. M. (1980) Selenium redox chemistry at GEOSECS I  
1025 re-occupation. *Earth Planet. Sci. Lett.* **49**, 102–108.

- 1026 Mitchell K., Mansoor S. Z., Mason P. R. D., Johnson T. M. and Van Cappellen P. (2016) Geological  
1027 evolution of the marine selenium cycle: Insights from the bulk shale  $\delta^{82/76}\text{Se}$  record and  
1028 isotope mass balance modeling. *Earth Planet. Sci. Lett.* **441**, 178–187.
- 1029 Mitchell K., Mason P. R., Van Cappellen P., Johnson T. M., Gill B. C., Owens J. D., Diaz J., Ingall E.  
1030 D., Reichart G.-J. and Lyons T. W. (2012) Selenium as paleo-oceanographic proxy: A first  
1031 assessment. *Geochim. Cosmochim. Acta* **89**, 302–317.
- 1032 Morford J. L. and Emerson S. (1999) The geochemistry of redox sensitive trace metals in  
1033 sediments. *Geochim. Cosmochim. Acta* **63**, 1735–1750.
- 1034 Mosher B. W. and Duce R. A. (1987). A global atmospheric selenium budget. *J. Geophys. Res.* **92**,  
1035 13289–13298.  
1036
- 1037 Oremland R. S., Hollibaugh J. T., Maest A. S., Presser T. S., Miller L. G. and Culbertson C. W.  
1038 (1989) Selenate reduction to elemental selenium by anaerobic bacteria in sediments  
1039 and culture: biogeochemical significance of a novel, sulfate-independent respiration.  
1040 *Appl Env. Microbiol.* **55**, 2333–2343.
- 1041 Over D. J. (1992) Conodonts and the Devonian–Carboniferous boundary in the upper Woodford  
1042 Shale, Arbuckle Mountains, south-central Oklahoma. *J. Paleontol.* **66**, 293–311.
- 1043 Over D. J. (2002) The Frasnian/Famennian boundary in central and eastern United States.  
1044 *Palaeogeogr. Palaeoclimatol. Palaeoecol.* **181**, 153–169.
- 1045 Partin C. A., Bekker A., Planavsky N. J., Scott C. T., Gill B. C., Li C., Podkovyrov V., Maslov A.,  
1046 Konhauser K. O., Lalonde S. V., Love G. D., Poulton S. W. and Lyons T. W. (2013) Large-  
1047 scale fluctuations in Precambrian atmospheric and oceanic oxygen levels from the  
1048 record of U in shales. *Earth Planet. Sci. Lett.* **369**, 284–293.
- 1049 Pogge von Strandmann P. A. E., Coath C. D., Catling D. C., Poulton S. W. and Elliott T. (2014)  
1050 Analysis of mass dependent and mass independent selenium isotope variability in black  
1051 shales. *J. Anal. At. Spectrom.* **29**, 1648–1659.
- 1052 Pogge von Strandmann P. A. E., Stüeken E. E., Elliott T., Poulton S. W., Dehler C. M., Canfield D.  
1053 E. and Catling D. C. (2015) Selenium isotope evidence for progressive oxidation of the  
1054 Neoproterozoic biosphere. *Nat. Commun.* **6**.
- 1055 Qie W. K., Algeo T. J., Luo G. M. and Herrmann A. D. (2019) Global events of the Early Devonian  
1056 to Middle Permian: A review. *Palaeogeogr. Palaeoclimatol. Palaeoecol.*,  
1057 <https://doi.org/10.1016/j.palaeo.2019.109259>.  
1058
- 1059 Roark A., Flake R., Grossman E. L., Olszewski T., Lebold J., Thomas D., Marcantonio F., Miller B.,  
1060 Raymond A. and Yancey T. (2017) Brachiopod geochemical records from across the

- 1061 Carboniferous seas of North America: Evidence for salinity gradients, stratification, and  
1062 circulation patterns. *Palaeogeogr. Palaeoclimatol. Palaeoecol.* **485**, 136–153.
- 1063 Rouxel O., Fouquet Y. and Ludden J. N. (2004) Subsurface processes at the Lucky Strike  
1064 hydrothermal field, Mid-Atlantic Ridge: evidence from sulfur, selenium, and iron  
1065 isotopes. *Geochim. Cosmochim. Acta* **68**, 2295–2311.
- 1066 Rovira M., Giménez J., Martínez M., Martínez-Lladó X., de Pablo J., Marti V. and Duro L. (2008)  
1067 Sorption of selenium (IV) and selenium (VI) onto natural iron oxides: goethite and  
1068 hematite. *J. Hazard. Mater.* **150**, 279–284.
- 1069 Rue E. L., Smith G. J., Cutter G. A. and Bruland K. W. (1997) The response of trace element redox  
1070 couples to suboxic conditions in the water column. *Deep Sea Res. Part Oceanogr. Res.*  
1071 *Pap.* **44**, 113–134.
- 1072 Sageman B. B., Murphy A. E., Werne J. P., Ver Straeten C. A., Hollander D. J. and Lyons T. W.  
1073 (2003) A tale of shales: the relative roles of production, decomposition, and dilution in  
1074 the accumulation of organic-rich strata, Middle–Upper Devonian, Appalachian basin.  
1075 *Chem. Geol.* **195**, 229–273.
- 1076 Schilling K., Johnson T. M. and Mason P. R. (2014) A sequential extraction technique for mass-  
1077 balanced stable selenium isotope analysis of soil samples. *Chem. Geol.* **381**, 125–130.
- 1078 Schilling K., Johnson T. M. and Wilcke W. (2011) Selenium partitioning and stable isotope ratios  
1079 in urban topsoils. *Soil Sci. Soc. Am. J.* **75**, 1354–1364.
- 1080 Scott C., Lyons T. W., Bekker A., Shen Y., Poulton S. W., Chu X. and Anbar A. D. (2008) Tracing  
1081 the stepwise oxygenation of the Proterozoic ocean. *Nature* **452**, 456–U5.
- 1082 Shiller A. M. (1996) The effect of recycling traps and upwelling on estuarine chemical flux  
1083 estimates. *Geochim. Cosmochim. Acta* **60**, 3177–3185.
- 1084 Shore A. J. T. (2011) Selenium geochemistry and isotopic composition of sediments from the  
1085 Cariaco Basin and the Bermuda Rise: a comparison between a restricted basin and the  
1086 open ocean over the last 500 ka. Ph.D. dissertation, University of Leicester, Leicester,  
1087 UK.
- 1088 Siebert C., Nagler T. F., von Blanckenburg F. and Kramers J. D. (2003). Molybdenum isotope  
1089 records as a potential new proxy for paleoceanography. *Earth Planet. Sci. Lett.* **211**, 159-  
1090 171.
- 1091  
1092 Sperling E. A., Frieder C. A., Raman A. V., Girguis P. R., Levin L. A. and Knoll A. H. (2013). Oxygen,  
1093 ecology, and the Cambrian radiation of animals. *Proc. Natl. Acad. Sci. (U. S. A.)* **110**,  
1094 13446-13451.
- 1095

- 1096 Stüeken E. E. (2017) Selenium isotopes as a biogeochemical proxy in deep time. *Rev. Mineral.*  
1097 *Geochem.* **82**, 657–682.
- 1098 Stüeken E. E., Buick R. and Anbar A. D. (2015a) Selenium isotopes support free O<sub>2</sub> in the latest  
1099 Archean. *Geology* **43**, 259–262.
- 1100 Stüeken E. E., Buick R., Bekker A., Catling D., Foriel J., Guy B. M., Kah L. C., Machel H. G.,  
1101 Montañez I. P. and Poulton S. W. (2015b) The evolution of the global selenium cycle:  
1102 Secular trends in Se isotopes and abundances. *Geochim. Cosmochim. Acta* **162**, 109–  
1103 125.
- 1104 Stüeken E. E., Catling D. C. and Buick R. (2012) Contributions to late Archean sulphur cycling by  
1105 life on land. *Nat. Geosci.* **5**, 722–725.
- 1106 Stüeken E. E., Foriel J., Buick R. and Schoepfer S. D. (2015c) Selenium isotope ratios, redox  
1107 changes and biological productivity across the end-Permian mass extinction. *Chem.*  
1108 *Geol.* **410**, 28–39.
- 1109 Stüeken E. E., Foriel J., Nelson B. K., Buick R. and Catling D. C. (2013) Selenium isotope analysis  
1110 of organic-rich shales: advances in sample preparation and isobaric interference  
1111 correction. *J. Anal. At. Spectrom.* **28**, 1734–1749.
- 1112 Stüeken E. E., Kipp M. A., Koehler M. C. and Buick R. (2016) The evolution of Earth's  
1113 biogeochemical nitrogen cycle. *Earth-Sci. Rev.* **160**, 220–239.
- 1114 Teng F.-Z., Watkins J. M., Dauphas N. and Swainson I. (2017) Non-Traditional Stable Isotopes.  
1115 *Rev Mineral. Geochem.* **82**, 885p.
- 1116 Tesdal J.-E., Galbraith E. D. and Kienast M. (2013) Nitrogen isotopes in bulk marine sediment:  
1117 linking seafloor observations with subseafloor records. *Biogeosciences* **10**, 101–118.
- 1118 Tissot F. L. and Dauphas N. (2015) Uranium isotopic compositions of the crust and ocean: Age  
1119 corrections, U budget and global extent of modern anoxia. *Geochim. Cosmochim. Acta*  
1120 **167**, 113–143.
- 1121 Tostevin R., Clarkson M. O., Gangl S., Shields G. A., Wood R. A., Bowyer F., Penny A. M. and  
1122 Stirling C. H. (2019) Uranium isotope evidence for an expansion of anoxia in terminal  
1123 Ediacaran oceans. *Earth Planet. Sci. Lett.* **506**, 104–112.
- 1124 Tribouillard N., Algeo T. J., Lyons T. and Riboulleau A. (2006) Trace metals as paleoredox and  
1125 paleoproductivity proxies: an update. *Chem. Geol.* **232**, 12–32.
- 1126 Turner A. C. E., Algeo T. J., Peng Y. and Herrmann A. D. (2019) Circulation patterns in the Late  
1127 Pennsylvanian North American Midcontinent Sea inferred from spatial gradients in  
1128 sediment chemistry and mineralogy. *Palaeogeogr. Palaeoclimatol. Palaeoecol.*,  
1129 <https://doi.org/10.1016/j.palaeo.2018.12.008>.

1130  
1131 Velinsky D. J. and Cutter G. A. (1990) Determination of elemental selenium and pyrite-selenium  
1132 in sediments. *Anal. Chim. Acta* **235**, 419–425.

1133 Ver Straeten C. A., Brett C. E. and Sageman B. B. (2011) Mudrock sequence stratigraphy: a  
1134 multi-proxy (sedimentological, paleobiological and geochemical) approach, Devonian  
1135 Appalachian Basin. *Palaeogeogr. Palaeoclimatol. Palaeoecol.* **304**, 54–73.

1136 Wei W. and Algeo T. J. (2019) Elemental proxies for paleosalinity analysis of ancient shales and  
1137 mudrocks. *Geochim. Cosmochim. Acta*, <https://doi.org/10.1016/j.gca.2019.06.034>.  
1138

1139 Wei W., Algeo T. J., Lu Y., Lu Y., Liu H., Zhang S., Peng L., Zhang J. and Chen L. (2018) Identifying  
1140 marine incursions into the Paleogene Bohai Bay Basin lake system in northeastern  
1141 China. *Int. J. Coal Geol.* **200**, 1–17.

1142 Wen H. J., Carignan J., Hu R. Z., Fan H. F., Bin C. and Yang G. S. (2007). Large selenium isotope  
1143 variations and its implication in the Yutangba Se deposit, Hubei Province, China. *Chinese  
1144 Science Bulletin.* **52**, 2443-2447.  
1145

1146 Werne J. P., Sageman B. B., Lyons T. W. and Hollander D. J. (2002) An integrated assessment of  
1147 a “type euxinic” deposit: evidence for multiple controls on black shale deposition in the  
1148 Middle Devonian Oatka Creek Formation. *Am. J. Sci.* **302**, 110–143.

1149 Wignall P. B. and Twitchett R. J. (1996). Oceanic Anoxia and the End Permian Mass Extinction.  
1150 *Science* **272**, 1155-1158.  
1151

1152 Yierpan A., Konig S., Labidi J., Kurzawa T., Babechuk M. G. and Schoenberg R. (2018). Chemical  
1153 Sample Processing for Combined Selenium Isotope and Selenium-Tellurium Elemental  
1154 Investigation of the Earth's Igneous Reservoirs. *Geochem. Geophys. Geosy.* **19**, 516-533.  
1155

1156 Zhang F., Algeo T. J., Romaniello S. J., Cui Y., Zhao L., Chen Z.-Q. and Anbar A. D. (2018)  
1157 Congruent Permian-Triassic  $\delta^{238}\text{U}$  records at Panthalassic and Tethyan sites:  
1158 Confirmation of global-oceanic anoxia and validation of the U-isotope paleoredox proxy.  
1159 *Geology* **46**, 327–330.

1160 Zhu J.-M., Johnson T. M., Clark S. K., Zhu X.-K. and Wang X.-L. (2014) Selenium redox cycling  
1161 during weathering of Se-rich shales: A selenium isotope study. *Geochim. Cosmochim.  
1162 Acta* **126**, 228–249.

1163

1164 **Table 1. Location information for the 10 study sections**

Section	Unit	Location	Curation <sup>a</sup>
C-TW-1	Tacket	Tulsa Co., OK: T22N, R13E, Sec. 6 SE-NE-NE-SW-SE; 36.416°N, 95.957°W	Oklahoma GS
KGS Edmonds #1A (ED)	Stark	Leavenworth Co., KS: T9S, R22E, Sec. 35 SE-SE-NW-SW; 39.220°N, 94.933°W	Kansas GS
KGS Edmonds #1A (ED)	Muncie Creek	Leavenworth Co., KS: T9S, R22E, Sec. 35 SE-SE-NW-SW; 39.220°N, 94.933°W	Kansas GS
ISGS #1 Englebart (EB)	Teutopolis	Jasper Co., IL: 40' FSL, 340' FEL, Sec. 9, T8N, R8E; 39.146°N, 88.318°W; elev. 575'	Illinois GS
Western New York Nuclear Fuel Service #1 [NX-1], also "West Valley core" (WVC)	Hanover-Dunkirk	Cattaraugus County, NY (42.4457°N, 78.6344°W)	New York GS
OHLO-2	Cleveland Member, Ohio Shale	Loraine County, OH (41.4001°N, 82.2438°W, elev. 683 ft)	Ohio GS
KEP-3	Cleveland Member, Ohio Shale	Lewis County, KY (38.409°N, 83.437°W)	Kentucky GS
Dupont HGS (DHGS)	Chattanooga	Humphreys County, TN (36.075°N, 87.495°W)	Tennessee GS
Ryan Shale Pit (RSP)	Woodford	Pontotoc County, OK (34.674°N, 96.641°W)	outcrop
Classen Lake YMCA (CLY)	Woodford	Murray County, OK (34.46°N, 97.15°W)	outcrop
Amoco A.J. Davis #9 (AJD)	Woodford	Yoakum County, TX (33.14°N, 102.89°W) Block D, Sec. 514, 2173 FSL, 1430 FEL; elev. 3710'; J.H. Gibson survey	Texas BEG
Thompson	Upper Bakken	Billings County, ND (47.229 °N, 103.263 °W)	North Dakota GS

1165 <sup>a</sup> GS = Geological Survey; BEG = Bureau of Economic Geology.

**Table 2. Geochemical data from late Pennsylvanian shales. Published data cited in footnotes.**

Unit	Sample ID	Se ( $\mu\text{g/g}$ )	$\delta^{82/78}\text{Se}$ ( $\text{‰}$ )	$\delta^{82/78}\text{Se}$ (95% CI)	TOC (wt. %)	TS (wt. %)	$\delta^{15}\text{N}$ ( $\text{‰}$ )	Al (wt. %)	Fe (wt. %)	Mo ( $\mu\text{g/g}$ )	DOP <sub>T</sub>
Muncie Creek	EDM 27-9	67.6	0.77	0.37	14.01 <sup>a</sup>	1.16 <sup>a</sup>	6.7 <sup>b</sup>	7.62 <sup>a</sup>	3.84 <sup>a</sup>	71.56 <sup>a</sup>	0.26 <sup>a</sup>
Muncie Creek	DMB-10	81.1	0.64	0.11	16.87 <sup>a</sup>	1.17 <sup>a</sup>	6.5 <sup>b</sup>	7.06 <sup>a</sup>	3.98 <sup>a</sup>	82.85 <sup>a</sup>	0.26 <sup>a</sup>
Muncie Creek	DMB-50	43.2	0.57	0.27	19.23 <sup>a</sup>	0.89 <sup>a</sup>	5.2 <sup>b</sup>	6.94 <sup>a</sup>	3.67 <sup>a</sup>	40.06 <sup>a</sup>	0.21 <sup>a</sup>
Muncie Creek	DMB-60	38.8	0.22	0.28	18.54 <sup>a</sup>	1.32 <sup>a</sup>	4.4 <sup>b</sup>	8.05 <sup>a</sup>	3.95 <sup>a</sup>	30.96 <sup>a</sup>	0.29 <sup>a</sup>
Muncie Creek	DMB-73	64.7	0.29	0.01	9.26 <sup>a</sup>	2.90 <sup>a</sup>	4.6 <sup>b</sup>	8.58 <sup>a</sup>	5.41 <sup>a</sup>	31.87 <sup>a</sup>	0.47 <sup>a</sup>
Stark	S-ED-X4	86.9	0.62	0.24	13.18 <sup>a</sup>	1.70 <sup>a</sup>	6.8	6.22 <sup>a</sup>	3.29 <sup>a</sup>	655.71 <sup>a</sup>	0.45 <sup>a</sup>
Stark	S-ED-X26	18.2	-0.11	0.26	6.54 <sup>a</sup>	1.39 <sup>a</sup>	5.6 <sup>b</sup>	8.56 <sup>a</sup>	3.86 <sup>a</sup>	7.89 <sup>a</sup>	0.31 <sup>a</sup>
Stark	S-ED-X28	16.3	-0.03	0.11	6.41 <sup>a</sup>	1.47 <sup>a</sup>	6.0 <sup>b</sup>	8.58 <sup>a</sup>	3.86 <sup>a</sup>	6.87 <sup>a</sup>	0.33 <sup>a</sup>
Stark	S-ED-X31	13.5	-0.07	0.34	4.40 <sup>a</sup>	1.87 <sup>a</sup>	5.7 <sup>b</sup>	8.58 <sup>a</sup>	4.37 <sup>a</sup>	5.33 <sup>a</sup>	0.37 <sup>a</sup>
Stark	S-ED-X32	10.4	-0.42	0.37	4.08 <sup>a</sup>	1.73 <sup>a</sup>	5.7 <sup>b</sup>	8.70 <sup>a</sup>	4.03 <sup>a</sup>	3.26 <sup>a</sup>	0.37 <sup>a</sup>
Stark	S-ED-X33	10.7	-0.78	0.26	2.09 <sup>a</sup>	2.25 <sup>a</sup>	6.1 <sup>b</sup>	8.76 <sup>a</sup>	4.54 <sup>a</sup>	3.53 <sup>a</sup>	0.43 <sup>a</sup>
Tacket	275.2	0.3	0.03		0.91 <sup>c</sup>	0.22 <sup>c</sup>	4.7	9.48 <sup>c</sup>	6.99 <sup>c</sup>	1.12 <sup>c</sup>	0.03 <sup>c</sup>
Tacket	216-222	41.9	0.03	0.18	9.45 <sup>c</sup>	8.78 <sup>c</sup>	6.1	6.47 <sup>c</sup>	6.77 <sup>c</sup>	14.10 <sup>c</sup>	0.97 <sup>c</sup>
Tacket	202.5- 205.0	33.6	-0.15	0.15	15.51 <sup>c</sup>	10.92 <sup>c</sup>	5.6	2.97 <sup>c</sup>	7.33 <sup>c</sup>	21.96 <sup>c</sup>	1.00 <sup>c</sup>
Tacket	174.0- 176.3	110.8	0.33	0.25	18.51 <sup>c</sup>	8.87 <sup>c</sup>	5.8	5.00 <sup>c</sup>	6.68 <sup>c</sup>	65.89 <sup>c</sup>	1.00 <sup>c</sup>
Tacket	132.0- 134.5	135.5	0.46	0.19	18.71 <sup>c</sup>	4.79 <sup>c</sup>	14.1	5.31 <sup>c</sup>	4.70 <sup>c</sup>	186.89 <sup>c</sup>	0.89 <sup>c</sup>
Tacket	84.5-87.5	6.6	-0.68	0.11	1.01 <sup>c</sup>	3.46 <sup>c</sup>	7.5	6.18 <sup>c</sup>	3.89 <sup>c</sup>	18.42 <sup>c</sup>	0.78 <sup>c</sup>
Tacket	57	22.9	-0.07	0.11	6.77 <sup>c</sup>	1.89 <sup>c</sup>	6.5	7.51 <sup>c</sup>	3.51 <sup>c</sup>	6.29 <sup>c</sup>	0.47 <sup>c</sup>
Teutopolis	5	0.6	-0.46	0.41	1.28 <sup>d</sup>	1.30 <sup>d</sup>	5.0	9.32 <sup>d</sup>	3.98 <sup>d</sup>	1.45 <sup>d</sup>	0.28 <sup>d</sup>
Teutopolis	15	0.7	-0.55		0.45 <sup>d</sup>	1.90 <sup>d</sup>	5.0	8.78 <sup>d</sup>	3.98 <sup>d</sup>	2.39 <sup>d</sup>	0.42 <sup>d</sup>

Teutopolis	35	1.0	-0.13	0.27	0.47 <sup>d</sup>	1.87 <sup>d</sup>	5.5	8.50 <sup>d</sup>	3.91 <sup>d</sup>	4.64 <sup>d</sup>	0.42 <sup>d</sup>
Teutopolis	45	1.0	-0.69	0.16	0.65 <sup>d</sup>	2.31 <sup>d</sup>	5.7	8.66 <sup>d</sup>	4.06 <sup>d</sup>	4.04 <sup>d</sup>	0.49 <sup>d</sup>
Teutopolis	55	2.2	-1.15	0.17	1.16 <sup>d</sup>	2.07 <sup>d</sup>	6.0				
Teutopolis	75	20.6	-0.29	0.30	9.89 <sup>d</sup>	3.27 <sup>d</sup>	6.8	8.40 <sup>d</sup>	6.03 <sup>d</sup>	24.64 <sup>d</sup>	0.47 <sup>d</sup>
Teutopolis	91	12.6	-0.58	0.23	4.82 <sup>d</sup>	2.50 <sup>d</sup>	6.2	7.65 <sup>d</sup>	4.5 <sup>d</sup>	19.64 <sup>d</sup>	0.48 <sup>d</sup>

1167 <sup>a</sup> Algeo and Maynard (2004); <sup>b</sup> Algeo et al. (2008b); <sup>c</sup> Algeo and Tribovillard (2009); <sup>d</sup> Turner et al. (2019).

**Table 3. Geochemical data from Late Devonian shales.** Published data cited in footnotes .

Unit	Sample ID	Se ( $\mu\text{g/g}$ )	$\delta^{82/78}\text{Se}$ (‰)	$\delta^{82/78}\text{Se}$ (95% CI)	TOC (wt. %)	TS (wt. %)	$\delta^{15}\text{N}$ (‰)
Dunkirk	WVC754-14	0.7	-0.24	0.75	1.89	2.20	0.6
Dunkirk	WVC754-2-5	0.4	-0.52		0.65	2.69	0.9
Hanover	WVC785-13	0.4	0.02		2.26	2.00	0.2
Hanover	WVC785-8	0.4	0.10		2.64	1.82	-0.5
Woodford	RSP-22	2.6	-0.30	0.35		0.44	
Woodford	RSP-40	8.2	-0.87	0.54		0.79	
Woodford	AJD-507	0.6	-0.36			0.52	
Woodford	AJD-513	1.1	-0.14			0.65	
Woodford	CLY-24	4.9	0.24	0.60		2.22	
Woodford	CLY-26	3.2	0.84	0.18		15.21	
Woodford	CLY-30	1.9	-0.25			1.53	
Woodford	CLY-33	2.4	-0.63	0.07		1.92	
Cleveland Member, Ohio Shale	OHLO-2_540'0'	1.1	1.00		7.94	3.67	0.0
Cleveland Member, Ohio Shale	OHLO-2_530'0'	0.8	0.60		7.02	2.68	-0.4
Cleveland Member, Ohio Shale	OHLO-2_519'9'	1.2	0.81	0.18	7.00	2.11	0.0
Cleveland Member, Ohio Shale	OHLO-2_510'0'	1.2	0.57	0.18	5.24	2.63	0.3
Cleveland Member, Ohio Shale	OHLO-2_469'7'	0.6	0.99		7.20	3.71	-0.3
Cleveland Member, Ohio Shale	OHLO-2_460'0'	0.7	0.75		5.72	5.13	-0.1
Cleveland Member, Ohio Shale	OHLO-2_309'3'	0.8	0.14		4.92	1.76	0.7
Chattanooga	Dup-75	2.2	0.37	0.82	10.36	5.80	1.9
Chattanooga	Dup-64	4.6	-0.38	0.17			
Chattanooga	Dup-54	2.7	1.55				
Chattanooga	Dup-60	2.0	0.93	0.21			
Chattanooga	Dup-33	3.8	-0.66	0.01			
Chattanooga	Dup-15	4.5	-0.06	0.26			
Cleveland Member, Ohio Shale	K3-17-9/2	2.9	0.17	0.25	2.66	2.41	2.0
Cleveland Member, Ohio Shale	K3-17-9/10	2.0	0.50	0.29	6.60	1.35	1.1

Cleveland Member, Ohio Shale	K3-12-8/9	24.3	-0.89	0.21	12.38	8.79	5.0
Cleveland Member, Ohio Shale	K3-12-8/4	37.0	-0.72	0.07	5.57	9.07	4.2
Cleveland Member, Ohio Shale	K3-12-8/3	8.6	0.23	0.14	11.55	1.53	4.6
Cleveland Member, Ohio Shale	K3-12-8/10	17.6	-0.26	0.01	12.84	2.68	5.1
Upper Bakken	T2-6	0.5	-0.04		0.96	3.10 <sup>c</sup>	1.5
Upper Bakken	T2-2	0.4	-0.96		0.92	3.40 <sup>c</sup>	1.5
Upper Bakken	T2-15	0.3	-0.44		0.60	3.00 <sup>c</sup>	1.8
Upper Bakken	T1-7	0.6	0.19		1.24	4.50 <sup>c</sup>	1.5
New Albany (anoxic)		0.5 <sup>a</sup>	0.91 <sup>a</sup>		8.60 <sup>b</sup>	3.79 <sup>b</sup>	0.2 <sup>d</sup>
New Albany (anoxic)		1.1 <sup>a</sup>	0.92 <sup>a</sup>		8.96 <sup>b</sup>	3.48 <sup>b</sup>	
New Albany (anoxic)		0.8 <sup>a</sup>	1.20 <sup>a</sup>		7.17 <sup>b</sup>	3.44 <sup>b</sup>	-0.1 <sup>d</sup>
New Albany (anoxic)		1.1 <sup>a</sup>	1.14 <sup>a</sup>		7.24 <sup>b</sup>	2.32 <sup>b</sup>	0.7 <sup>d</sup>
New Albany (anoxic)		1.0 <sup>a</sup>	1.52 <sup>a</sup>		11.83 <sup>b</sup>	3.30 <sup>b</sup>	-0.1 <sup>d</sup>
New Albany (oxic)		0.5 <sup>a</sup>	0.47 <sup>a</sup>		0.31 <sup>b</sup>	0.56 <sup>b</sup>	1.5 <sup>d</sup>
New Albany (oxic)		1.0 <sup>a</sup>	0.45 <sup>a</sup>		0.48 <sup>b</sup>	1.63 <sup>b</sup>	2.2 <sup>d</sup>
New Albany (oxic)		0.8 <sup>a</sup>	0.64 <sup>a</sup>		0.13 <sup>b</sup>	1.19 <sup>b</sup>	2.9 <sup>d</sup>
New Albany (oxic)		0.6 <sup>a</sup>	0.48 <sup>a</sup>		0.18 <sup>b</sup>	0.42 <sup>b</sup>	2.6 <sup>d</sup>
New Albany (oxic)		0.4 <sup>a</sup>	0.19 <sup>a</sup>		0.38 <sup>b</sup>	1.39 <sup>b</sup>	2.9 <sup>d</sup>

1169  
1170

<sup>a</sup> Mitchell et al. (2012); <sup>b</sup> Ingall et al. (1993); <sup>c</sup> Hartwell (1998); <sup>d</sup> Calvert et al. (1996).

1171 **Table 4. Unit-average Mo/TOC and Sr/Ba data for Late Devonian units.**

Section	Formation	Mo/TOC <sup>a</sup> (10 <sup>4</sup> * g/g)	Sr/Ba <sup>b,c</sup> (g/g)
RSP, CLY, AJD	Woodford	23.4 ± 1.7	0.34 ± 0.14
Thompson	Upper Bakken	13.2 ± 1.5	0.29 ± 0.08
WVC	Hanover-Dunkirk	11.6 ± 6.1	0.26 ± 0.05
KEP-3	Cleveland Member, Ohio Shale	13.9 ± 6.9	0.23 ± 0.02
DHGS	Chattanooga	7.0 ± 5.4	0.45 ± 0.09
INJK-13	Camp Run Member, New Albany (oxic)	N/A	0.24 ± 0.06
INJK-13	Camp Run Member, New Albany (anoxic)	4.5 ± 0.5	0.16 ± 0.04

1172 <sup>a</sup> Mo/TOC data from [Algeo et al. \(2007\)](#) except West Valley and Chattanooga ([this study](#)) and presented ±1σ.

1173 <sup>b</sup> Sr/Ba data from [Liu and Algeo \(2019\)](#) except New Albany ([Calvert et al., 1996](#)).

1174 <sup>c</sup> Samples with >5 wt. % CaCO<sub>3</sub> were excluded from calculation due to contamination of signal with carbonate-bound Sr.

1175 **Figure Legends**

1176

1177 **Figure 1. Redox potentials of redox couplets commonly utilized in paleo-redox studies.** Data  
1178 generated for a pH range of 7-8. Dashed lines denote stability field of liquid water. Reduction of  
1179 selenium oxyanions begins at relatively high redox potentials, similar to the range for iodate and  
1180 nitrate reduction (Rue et al., 1997).

1181

1182 **Figure 2. Paleogeographic reconstruction of North America in the (A) Late Pennsylvanian and**  
1183 **(B) Late Devonian.** All sample sites are denoted with labeled points. Grey bands denote  
1184 submarine topographic highs separating basins. Maps were modified from Turner et al. (2019)  
1185 and Algeo et al. (2007), respectively.

1186

1187 **Figure 3. Boxplot of (A)  $\delta^{82/78}\text{Se}$ , (B) Se (EF), (C) TOC (wt. %), (D) TS. (wt. %), (E) TOC/TS (wt.**  
1188 **%/wt. %), (F)  $\delta^{15}\text{N}$ , (G) Fe/Al (g/g), (H) degree of pyritization ( $\text{DOP}_T$ ), (I) Mo/TOC ( $10^4 * \text{g/g}$ ) and**  
1189 **(J) Sr/Ba (g/g) for Late Pennsylvanian units.** In panel A, upper crust composition is denoted with  
1190 black dashed line; modern seawater composition is noted with red dotted line. The Sr/Ba values  
1191 for Stark shale were calculated from 11 samples sitting 0-40 cm above the samples measured for  
1192 Se isotopes. In this and subsequent boxplots, boxes are drawn as the limits of the first and third  
1193 quartiles, whiskers comprise the 95% confidence interval, and black lines denote the median.

1194

1195 **Figure 4. Relationship between Se and Mo in Late Pennsylvanian units.** (A) Se ( $\mu\text{g/g}$ ) vs. Mo/TOC  
1196 and (B) Se (EF) vs. Mo (EF). Coloration of data points denotes  $\delta^{82/78}\text{Se}$  values, with darker shading  
1197 indicative of higher values. The positive correlation between Se enrichment and Mo/TOC in units  
1198 *within* the Midcontinent Shelf environment suggests that the same mechanism was  
1199 concentrating both trace metals. This is consistent with the nutrient-trap mechanism proposed  
1200 by Algeo and Herrmann (2018). Furthermore, Se was being enriched relative to Mo by the  
1201 nutrient trap, as evidenced by higher enrichment factors (EF) across the Midcontinent Shelf. The  
1202 bottom waters that overlay the Teutopolis Shale in the Illinois Basin were isolated from exchange  
1203 with the Midcontinent Shelf, thus giving distinct Se ( $\mu\text{g/g}$ ) vs. Mo/TOC and Se (EF) vs. Mo (EF)  
1204 trends with smaller Se enrichments.

1205

1206 **Figure 5. Boxplot of (A)  $\delta^{82/78}\text{Se}$  values, (B) Sr/Ba, (C) unit-averaged Mo/TOC, (D) TOC/TS (wt.**  
1207 **%/wt. %), (E) Se ( $\mu\text{g/g}$ ) and (F)  $\delta^{15}\text{N}$  in Late Devonian units.** In panel A, upper crust composition  
1208 is denoted with black dashed line; modern seawater composition is noted with red dotted line.  
1209 Unlike in the NAMS black shales,  $\delta^{82/78}\text{Se}$  values do not closely correlate with TOC/TS. On the  
1210 contrary, Mo/TOC and  $\delta^{15}\text{N}$  show similar trajectories to the  $\delta^{82/78}\text{Se}$  values.

1211

1212 **Figure 6. Correlation between (A)  $\delta^{82/78}\text{Se}$  and TOC/TS, (B)  $\delta^{82/78}\text{Se}$  and  $\delta^{15}\text{N}$ , and (C) Se ( $\mu\text{g/g}$ )**  
1213 **and  $\delta^{15}\text{N}$  in Late Devonian units.** The relatively weak correlation between  $\delta^{82/78}\text{Se}$  and TOC/TS  
1214 suggests that other factors altered the isotopic composition of the organic- and/or sulfide-bound  
1215 Se fractions. The moderate negative correlation between  $\delta^{82/78}\text{Se}$  and  $\delta^{15}\text{N}$  suggests that some  
1216 portion of the Se oxyanion pool was being removed at high redox potentials similar to that of  
1217 nitrate reduction. The muted Se concentrations in settings with near-zero  $\delta^{15}\text{N}$  values suggest

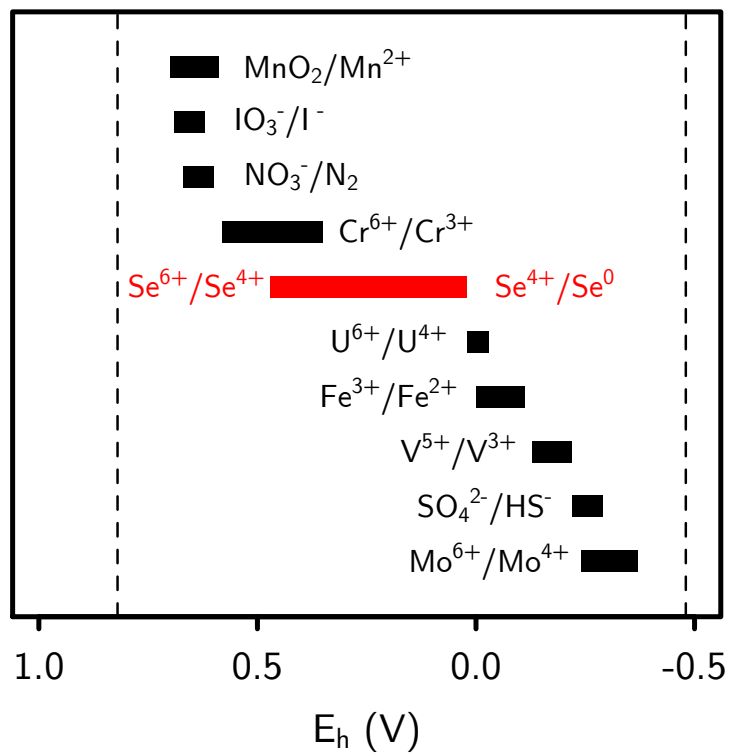
1218 that depletion of the nitrate and Se oxyanion reservoirs was indeed concurrent. In contrast, the  
1219 higher Se concentrations are found in samples with more positive  $\delta^{15}\text{N}$  values, consistent with  
1220 the presence of nitrate (and Se oxyanions) in the water column.

1221  
1222 **Figure 7. Negative correlation between unit-averaged  $\delta^{82/78}\text{Se}$  and Mo/TOC in Late Devonian**  
1223 **units.** More negative  $\delta^{82/78}\text{Se}$  values are found in units with higher Mo/TOC ratios, suggesting  
1224 faster seawater replenishment, which may have enabled non-quantitative Se oxyanion  
1225 reduction.

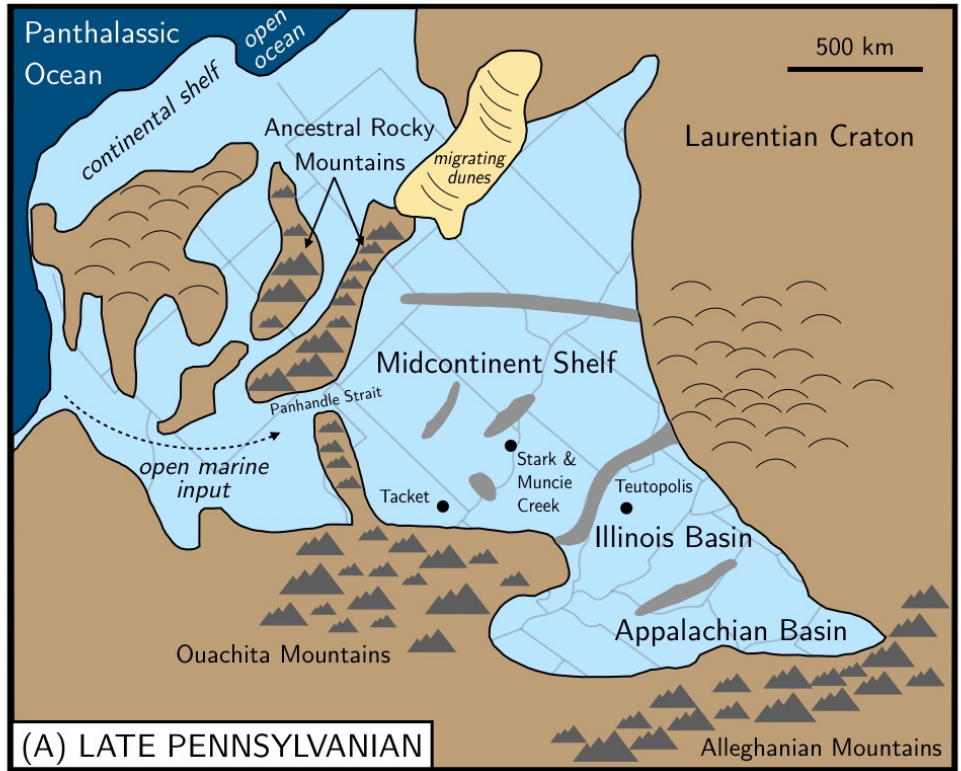
1226  
1227 **Figure 8. Differences in redox, hydrography and Se cycling between the Late Pennsylvanian**  
1228 **NAMS and the Late Devonian NAS.** Low Se concentrations in the NAS are likely the result of  
1229 basal restriction (evidenced by low Sr/Ba ratios) and Se oxyanion depletion (suggested by low  
1230  $\delta^{15}\text{N}$  values, which imply nitrate depletion). The difference in Se concentrations between the  
1231 NAMS and NAS is not due to differing TOC or TS contents, suggesting that the controls have to  
1232 do with watermass circulation and seawater renewal instead of local bottom-water redox  
1233 conditions.

1234  
1235 **Figure 9. Selenium enrichment factors relative to molybdenum (A), uranium (B) and vanadium**  
1236 **(C).** The greater enrichment of Se relative to other redox-sensitive trace metals in the NAMS  
1237 shales suggests that Se was more effectively recycled by the estuarine nutrient trap. In contrast,  
1238 Se is not preferentially enriched relative to U and V in the NAS black shales, which did not feature  
1239 a nutrient trap. The higher Mo enrichment relative to Se in the NAS samples may reflect depletion  
1240 of the aqueous Se reservoir faster than the Mo reservoir at redox potentials higher than that  
1241 required for Mo scavenging (*i.e.*, euxinic conditions).

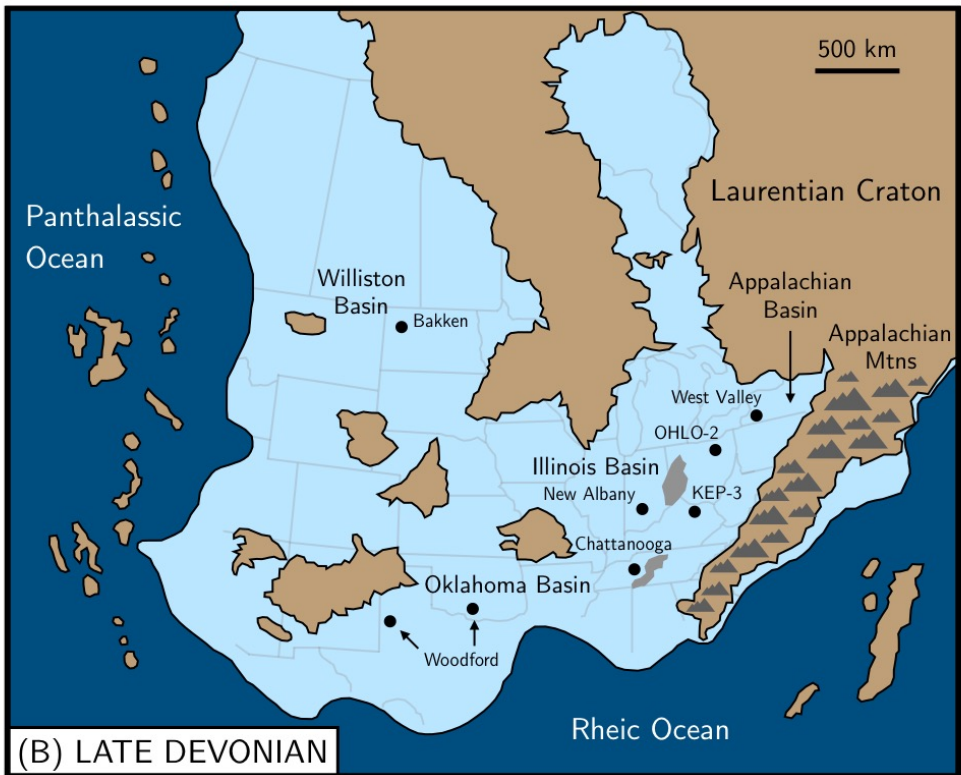
1242  
1243



1244  
 1245 **Figure 1.**  
 1246

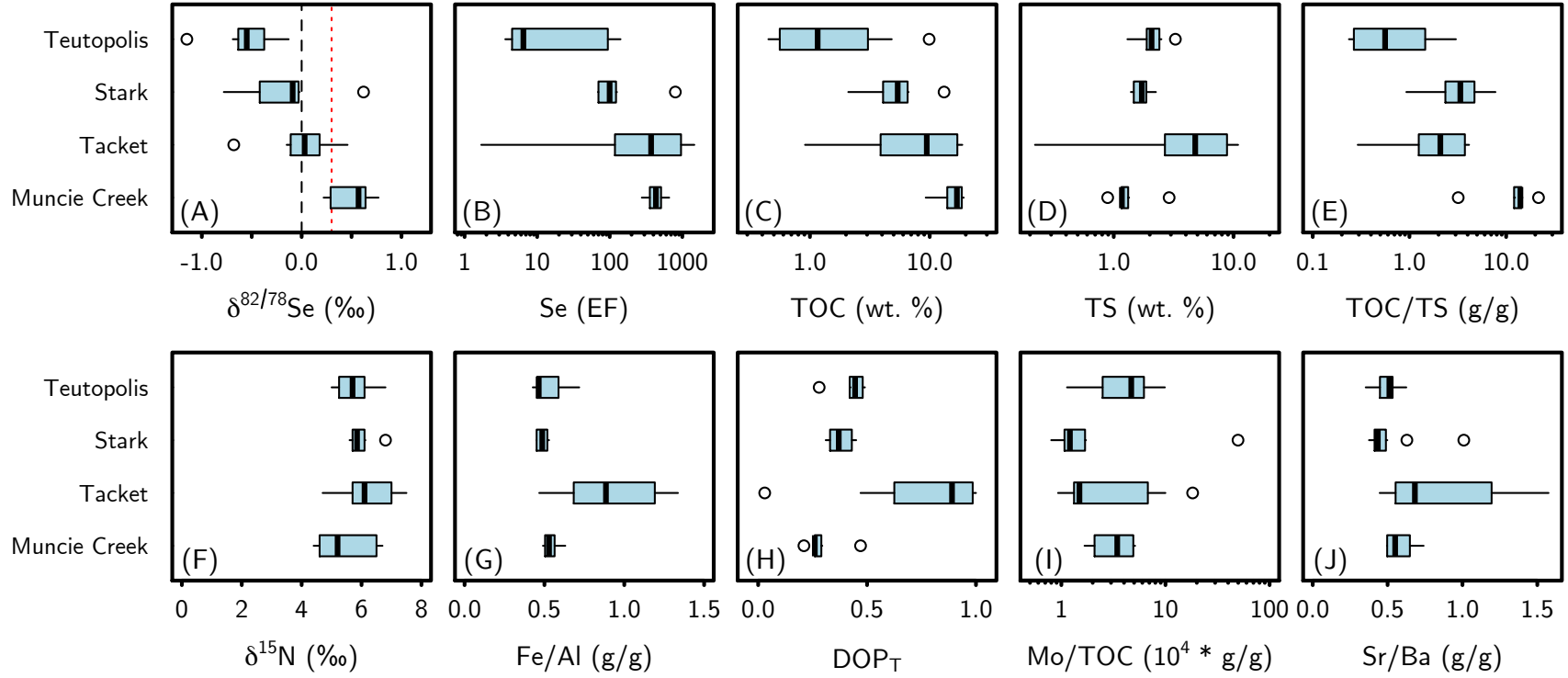


1247



1248  
1249  
1250  
1251

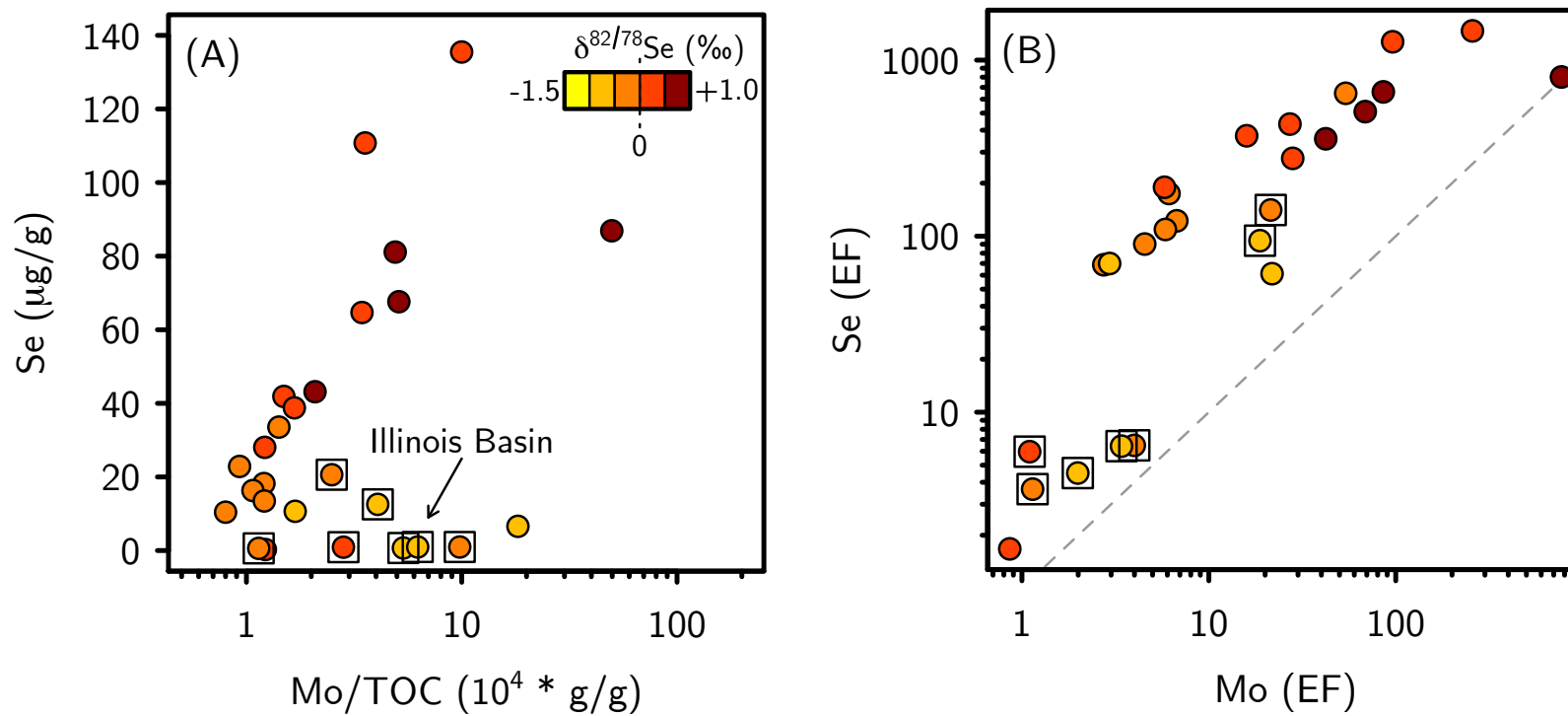
Figure 2.



1252  
1253

**Figure 3.**

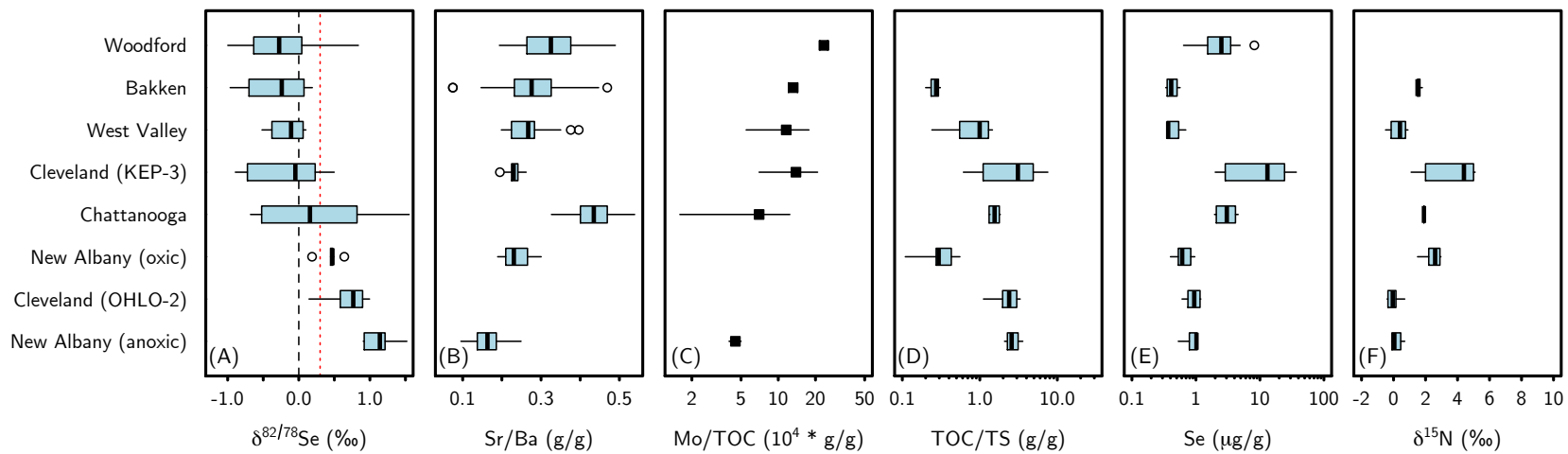
1254  
1255



1256  
1257  
1258

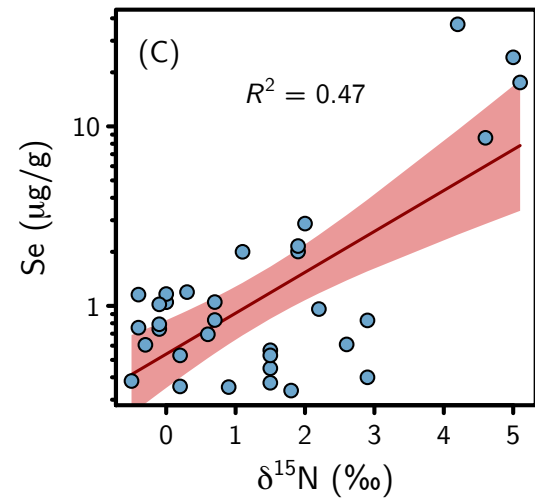
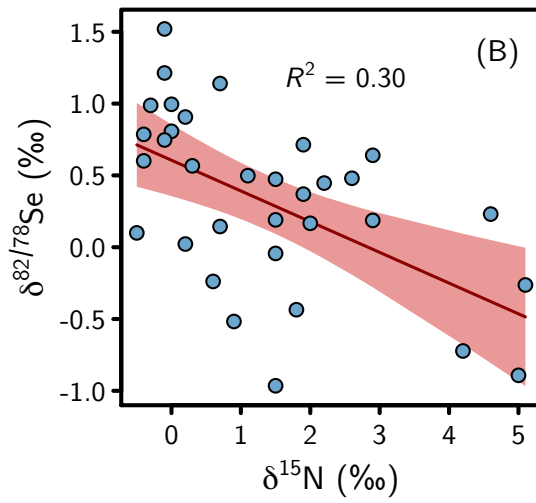
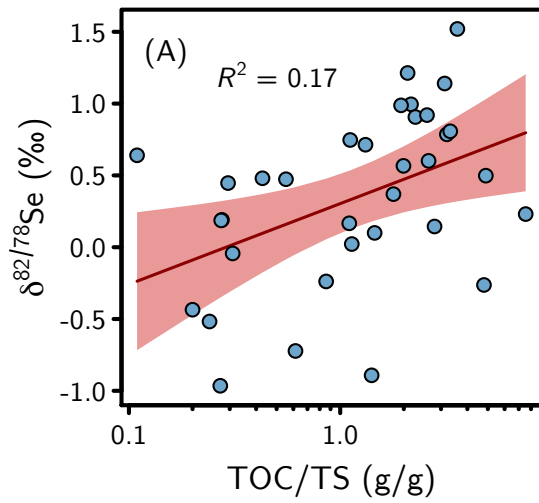
Figure 4.





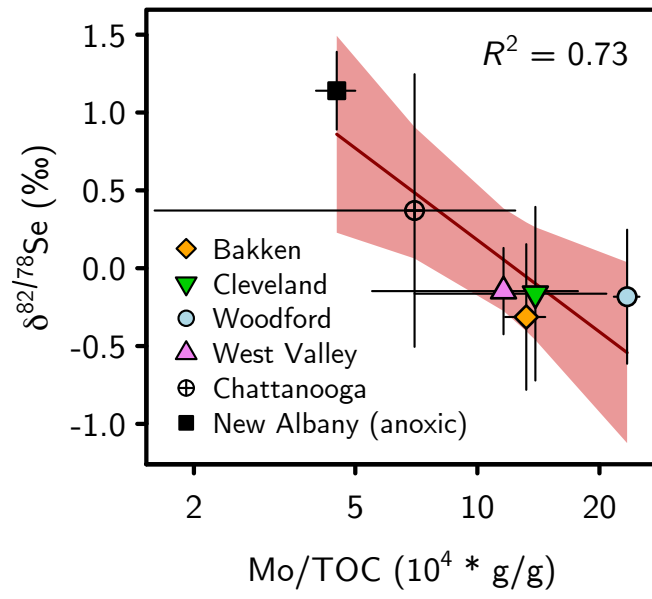
1260  
1261  
1262

**Figure 5.**



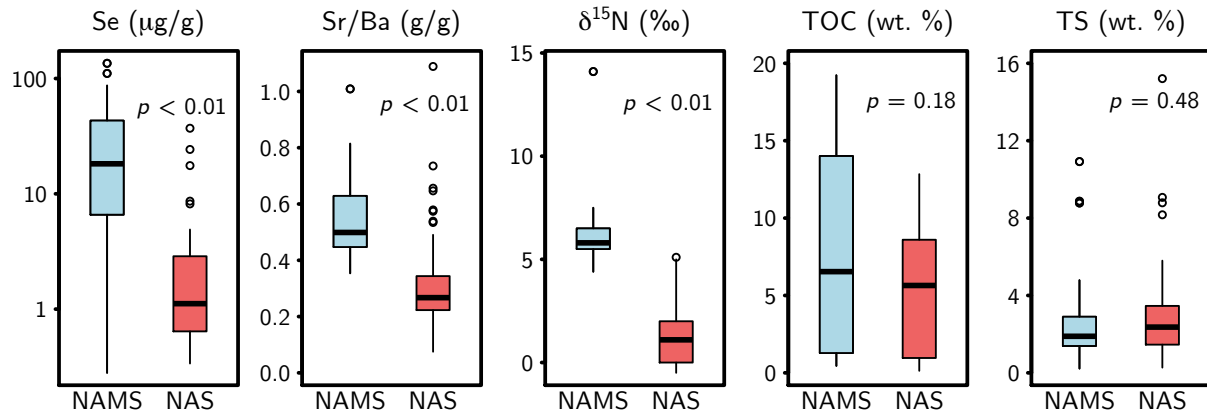
1263  
1264

Figure 6.



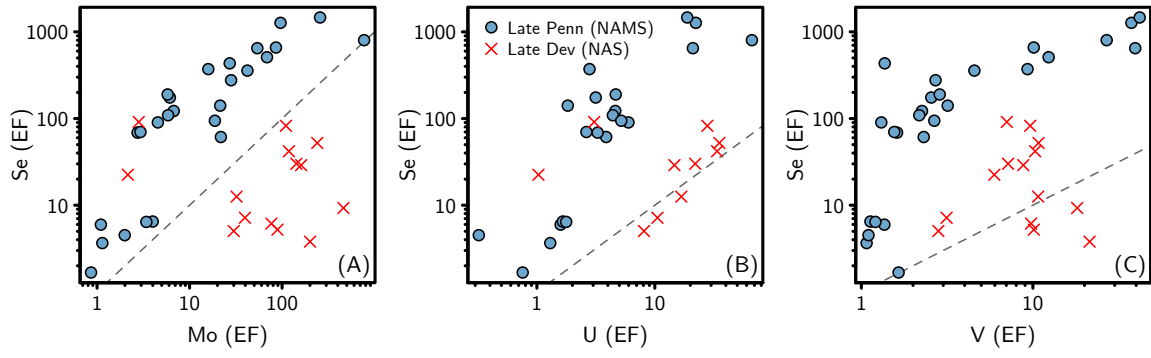
1265  
1266

Figure 7.



1267  
 1268  
 1269  
 1270

**Figure 8.**



1271  
1272

**Figure 9.**